



UNIVERSITY OF LEEDS

This is a repository copy of *The 12 November 2017 Mw 7.3 Ezgeleh-Sarpolzahab (Iran) Earthquake and Active Tectonics of the Lurestan Arc*.

White Rose Research Online URL for this paper:
<http://eprints.whiterose.ac.uk/141427/>

Version: Published Version

Article:

Nissen, E, Ghods, A, Karasözen, E et al. (12 more authors) (2019) The 12 November 2017 Mw 7.3 Ezgeleh-Sarpolzahab (Iran) Earthquake and Active Tectonics of the Lurestan Arc. *Journal of Geophysical Research: Solid Earth*, 124 (2). pp. 2124-2152. ISSN 2169-9356

<https://doi.org/10.1029/2018JB016221>

Reuse

Items deposited in White Rose Research Online are protected by copyright, with all rights reserved unless indicated otherwise. They may be downloaded and/or printed for private study, or other acts as permitted by national copyright laws. The publisher or other rights holders may allow further reproduction and re-use of the full text version. This is indicated by the licence information on the White Rose Research Online record for the item.

Takedown

If you consider content in White Rose Research Online to be in breach of UK law, please notify us by emailing eprints@whiterose.ac.uk including the URL of the record and the reason for the withdrawal request.



eprints@whiterose.ac.uk
<https://eprints.whiterose.ac.uk/>

RESEARCH ARTICLE

10.1029/2018JB016221

The 12 November 2017 M_w 7.3 Ezgeleh-Sarpolzahab (Iran) Earthquake and Active Tectonics of the Lurestan Arc

Key Points:

- The M_w 7.3 Ezgeleh-Sarpolzahab earthquake ruptured a gently dipping oblique fault in the Lurestan arc basement
- This faulting may be pervasive across the Lurestan arc, though it is unlikely seismogenic everywhere
- Relocated aftershocks correlate strongly with directivity implying a component of dynamic triggering

Supporting Information:

- Supporting Information S1

Correspondence to:

E. Nissen,
enissen@uvic.ca

Citation:

Nissen, E., Ghods, A., Karasözen, A., Elliott, J. R., Barnhart, W. D., Bergman, E. A., et al. (2019). The 12 November 2017 M_w 7.3 Ezgeleh-Sarpolzahab (Iran) earthquake and active tectonics of the Lurestan arc. *Journal of Geophysical Research: Solid Earth*, 124, 2124–2152. <https://doi.org/10.1029/2018JB016221>

Received 12 JUN 2018

Accepted 18 JAN 2019

Accepted article online 25 JAN 2019

Published online 16 FEB 2019

Edwin Nissen^{1,2} , Abdolreza Ghods³, Ezgi Karasözen² , John R. Elliott⁴ , William D. Barnhart⁵ , Eric A. Bergman⁶ , Gavin P. Hayes⁷ , Mohammadreza Jamal-Reyhani³, Majid Nemati⁸, Fengzhou Tan¹ , Wathiq Abdulnaby⁹, Harley M. Benz⁷ , Mohammad P. Shahvar¹⁰, Morteza Talebian¹¹, and Ling Chen¹² 

¹School of Earth and Ocean Sciences, University of Victoria, Victoria, British Columbia, Canada, ²Department of Geophysics, Colorado School of Mines, Golden, CO, USA, ³Department of Earth Sciences, Institute for Advanced Studies in Basic Sciences, Zanjan, Iran, ⁴COMET, School of Earth and Environment, University of Leeds, Leeds, UK, ⁵Department of Earth and Environmental Sciences, University of Iowa, Iowa City, IA, USA, ⁶Global Seismological Services, Golden, CO, USA, ⁷National Earthquake Information Center, U. S. Geological Survey, Golden, CO, USA, ⁸Department of Geology and Earthquake Research Center, Shahid Bahonar University of Kerman, Kerman, Iran, ⁹Geology Department, College of Science, University of Basrah, Basrah, Iraq, ¹⁰Road, Housing and Urban Development Research Center, Building and Housing Research Network, Tehran, Iran, ¹¹Research Institute for Earth Sciences, Geological Survey of Iran, Tehran, Iran, ¹²Institute of Geology and Geophysics, Chinese Academy of Sciences, Beijing, China

Abstract The 12 November 2017 M_w 7.3 Ezgeleh-Sarpolzahab earthquake is the largest instrumentally recorded earthquake in the Zagros Simply Folded Belt by a factor of ~ 10 in seismic moment. Exploiting local, regional, and teleseismic data and synthetic aperture radar interferometry imagery, we characterize the rupture, its aftershock sequence, background seismicity, and regional tectonics. The mainshock ruptured slowly (~ 2 km/s), unilaterally southward, for ~ 40 km along an oblique (dextral-thrust) fault that dips $\sim 14^\circ$ E beneath the northwestern Lurestan arc. Slip is confined to basement depths of ~ 12 – 18 km, resolvably beneath the sedimentary cover which is ~ 8 km thick in this area. The gentle dip angle and basement location allow for a broad slip area, explaining the large magnitude relative to earthquakes in the main Fars arc of the Zagros, where shallower, steeper faults are limited in rupture extent by weak sedimentary layers. Early aftershocks concentrate around the southern and western edges of the mainshock slip area and therefore cluster in the direction of rupture propagation, implying a contribution from dynamic triggering. A cluster of events ~ 100 km to the south near Mandali (Iraq) reactivated the $\sim 50^\circ$ dipping Zagros Foredeep Fault. The basement fault responsible for the Ezgeleh-Sarpolzahab earthquake probably accounts for the ~ 1 km elevation contrast between the Lurestan arc and the Kirkuk embayment but is distinct from sections of the Mountain Front Fault that define frontal escarpments elsewhere in the Zagros. It may be related to a seismic interface underlying the central and southern Lurestan arc, and a key concern is whether or not the more extensive regional structure is also seismogenic.

1. Introduction

The Zagros range in southwestern Iran is an archetype fold-and-thrust belt at the leading edge of the Arabia-Eurasia continental collision zone (Figure 1a), which accommodates approximately one third of its overall ~ 20 to 30 mm/year convergence rate (Vernant et al., 2004). Within the Zagros, an ~ 8 to 14 km-thick sequence of Phanerozoic sediments is folded and faulted in response to this collision, with active shortening focused within the frontal part of the range, known as the Simply Folded Belt (SFB; Walpersdorf et al., 2006). This is further subdivided along-strike into the mountainous Lurestan and Fars arcs, the lower-lying Kirkuk and Dezful embayments, and the sharp southeastern Oman syntaxis (Figure 2a). The SFB is unusual among major continental plate boundary zones in the complete absence of surface-rupturing earthquakes. It is characterized by a large number of moderate (M_w 5–6) earthquakes, mostly with shallow (~ 5 – 10 km) centroid depths consistent with rupture within the sedimentary cover (Nissen et al., 2011; Figures 1a and 2). Prior to 2017, the instrumental record lacked earthquakes larger than M_w 6.7, in stark contrast with many other regions of Iran where $M_w > 7$, surface-rupturing earthquakes are well known (e.g., Berberian & Yeats, 1999).

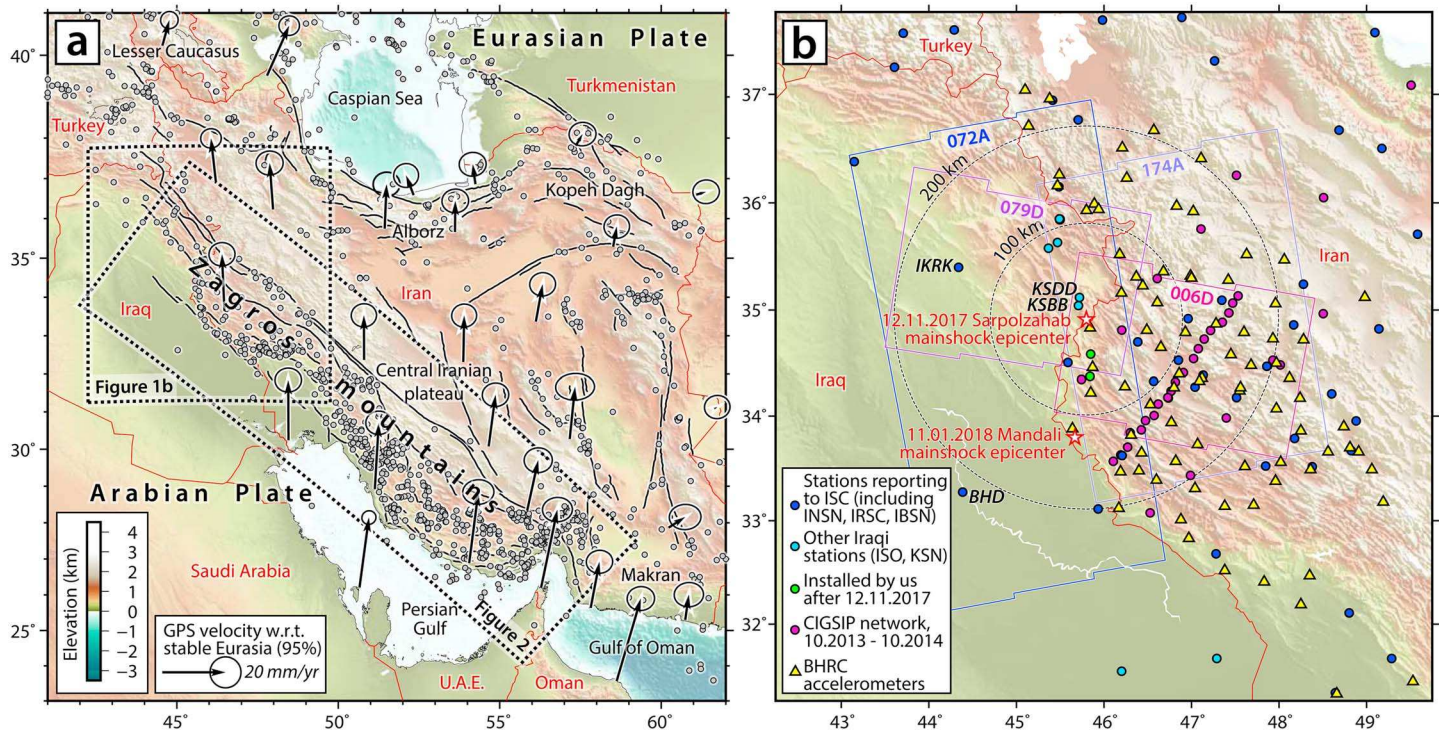


Figure 1. (a) Tectonic setting of the Zagros Mountains. Gray circles show $M > 5$ earthquake epicenters from the International Seismological Centre Bulletin (spanning 1909–2018), black lines show major active faults, and vectors show GPS velocities in a stable Eurasia reference frame (Vernant et al., 2004). (b) Regional station coverage used for earthquake relocations and first motions focal mechanisms (see text for details), and the extents of Sentinel interferograms used to study the 2017 Sarpolzahab mainshock, labeled by track number (interferograms from tracks 072A and 006D used to study the 2018 Mandali earthquakes are not shown).

This may reflect the compartmentalization of steep reverse faults by weak evaporitic layers in the lower to middle sedimentary cover, limiting downdip rupture widths for shallow earthquakes (Copley et al., 2015; Elliott et al., 2015; Koyi et al., 2000; Nissen et al., 2011). The seismicity accounts for a relatively minor (up to ~20%) proportion of the known geodetic deformation (Barnhart et al., 2013; Masson et al., 2005; Palano et al., 2018), with the remainder likely accounted for by folding of sedimentary rocks, aseismic fault slip (Barnhart & Lohman, 2013), and ductile shortening of the basement (Allen et al., 2013).

On 12 November 2017 at 18:18 UTC, a M_w 7.3 earthquake struck the northwestern SFB, with an epicenter near the Iranian town of Ezelgeh, a few kilometers east of the border with Iraq in the western Lurestan arc. More than 600 people were killed, mostly in Sarpolzahab, a larger Iranian town (population ~90,000) ~50 km south of Ezgeleh. Villages of the Zahab plain, north of Sarpolzahab, also suffered very heavy damage. We refer to the event as the Ezgeleh-Sarpolzahab earthquake, though elsewhere it has been termed the Darbandikhan earthquake after the Iraqi town ~35 km NW of Ezgeleh (Barnhart et al., 2018). The earthquake was surprising in that its moment is about 10 times that of the previous largest instrumental earthquakes in the SFB, the 1972 Ghir and 1977 Khurgu earthquakes, both M_w 6.7 reverse faulting events in the Fars arc; there are no clear historical examples of earthquakes exceeding $M \sim 7$ in the SFB either (Ambraseys & Melville, 1982). The mechanism of the Ezgeleh-Sarpolzahab mainshock is also rather unusual, with automated solutions from the U.S. Geological Survey (USGS) and Global Centroid Moment Tensor (GCMT) catalogs both indicating oblique dextral-reverse slip on a gentle (11–19°) east dipping fault plane or oblique sinistral-reverse slip on a steep (79–89°) SSW dipping plane (Table 1). Previously, most of the largest earthquakes in the SFB have involved predominantly reverse slip on moderately dipping (~20–60° dipping) fault planes (Nissen et al., 2011; Talebian & Jackson, 2004). Furthermore, neither nodal plane aligns closely with blind thrust faults inferred in this region, which are shown dipping toward the NE (Berberian, 1995).

The aims of this paper are twofold. (1) First, we document the source characteristics of the Ezgeleh-Sarpolzahab mainshock and its early aftershocks (up to 1 April 2018) using a comprehensive set of seismic and geodetic data. This not only includes freely available synthetic aperture radar interferometry

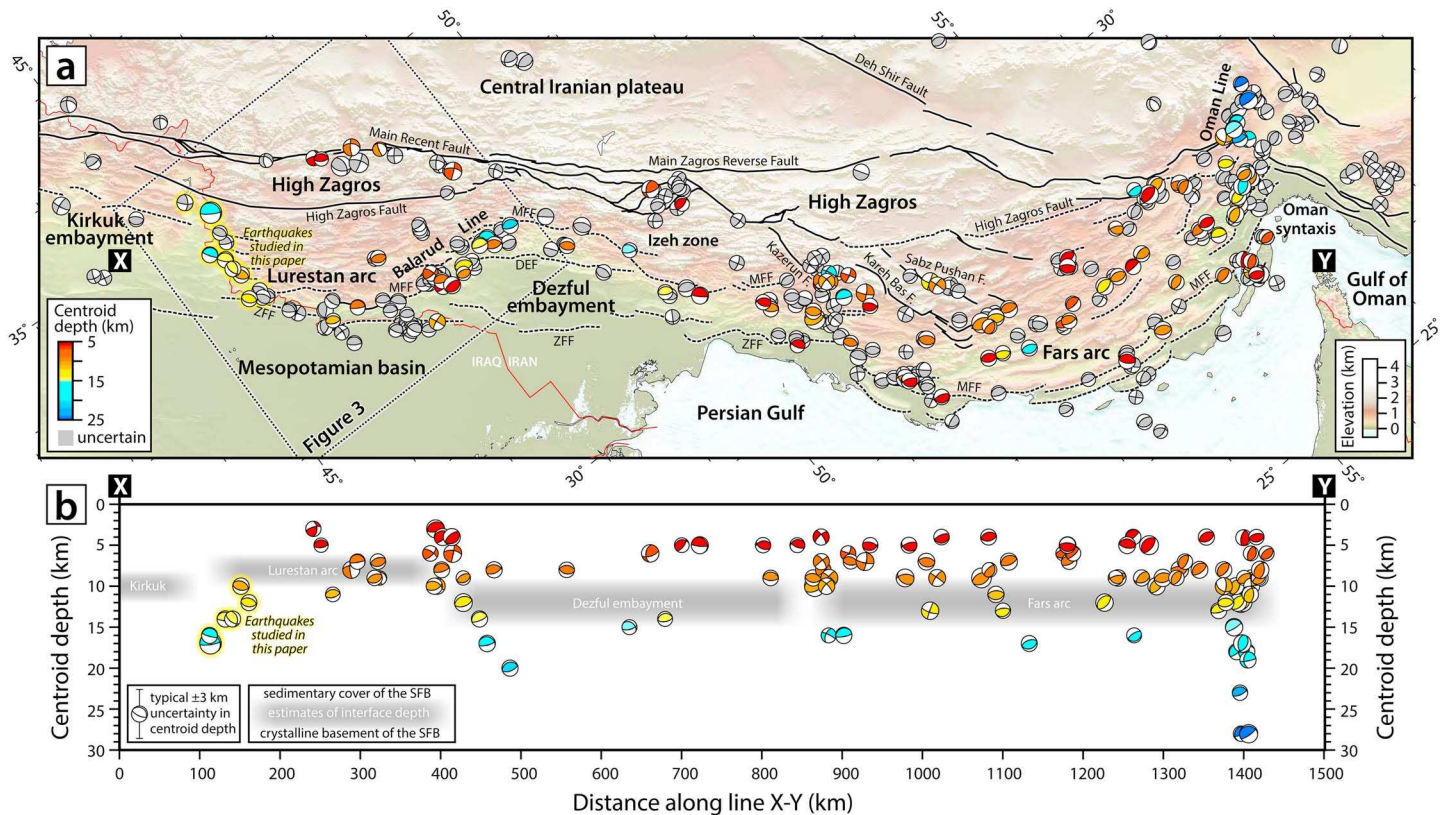


Figure 2. (a) Active faults and earthquake focal mechanisms of the Zagros in an oblique Mercator projection with equator azimuth N130°E. Black lines are faults; surface projections of Berberian's (1995) "master blind thrusts" are dashed (DEF = Dezful Embayment Fault; MFF = Mountain Front Fault; ZFF = Zagros Foredeep Fault). Focal mechanisms are from the period 1957–2018 and magnitude range $M_w > \sim 5$. Events modeled with long-period teleseismic body waveforms are colored by centroid depth, updated from Nissen et al. (2011); yellow haloes highlight those from this paper. Earthquakes lacking robust estimates of centroid depth (mostly early instrumental first motions mechanisms and Global Centroid Moment Tensor catalog solutions) are in gray. (b) Earthquake mechanisms plotted by centroid depth and projected distance along the line X-Y in (a). Ranges of basement depth estimates for the SFB are shown in gray (see text for references); note that the basement in the High Zagros is substantially shallower than in the SFB. SFB = Simply Folded Belt.

(InSAR) and teleseismic waveform data but also local and regional phase picks and waveforms that are not widely accessible (Figure 1b). Though we are aware of interesting aseismic processes initiated by the mainshock, including shallow bedding plane slip, postseismic deformation (Barnhart et al., 2018), and landsliding, the strong focus of this paper is on the seismic aspects of the sequence. (2) Second, we use the mainshock, its aftershocks, and a few previous earthquakes to investigate the regional tectonics. Since the advent of InSAR, large SFB earthquakes have concentrated within the Fars arc (Barnhart & Lohman, 2013; Elliott et al., 2015; Lohman & Barnhart, 2010; Lohman & Simons, 2005; Nissen et al., 2007, 2010; Roustaei et al., 2010) and so the Ezgeleh-Sarpolzahab sequence could help illuminate a relatively poorly understood part of the Zagros orogen. The Lurestan arc has several characteristics that distinguish it from other parts of the SFB, including a relatively slow and highly oblique plate convergence vector of $\sim 4\text{--}6$ mm/year with respect to central Iran (Vernant et al., 2004; Walpersdorf et al., 2006), a thinner sedimentary cover of ~ 8 km that may lack basal salt (Vergés, Goodarzi, et al., 2011), and a distinctive crustal and lithospheric structure (Motaghi, Shabanian & Kalvandi 2017; Vergés, Saura, et al., 2011). A principle concern arising from the M_w 7.3 Ezgeleh-Sarpolzahab earthquake is whether events of similar magnitude could occur elsewhere in the Zagros, or whether this style of earthquake results from attributes unique to Lurestan.

2. Geology, Structure, and Tectonics of the Lurestan Arc

In this section we review the geology of the Lurestan arc, which in other parts of the SFB exerts a strong influence on seismicity and earthquake faulting (e.g., Elliott et al., 2015; Nissen et al., 2011). We also summarize its crustal structure, past earthquake activity, and structural relations with the neighboring Kirkuk and Dezful embayments.

Table 1
Source Parameters of the 12 November 2017 (18:18 UTC) Ezgeleh-Sarpolzahab Mainshock

Source	Data	Strike	Dip	Rake	SV	Longitude	Latitude	Depth	Seismic moment	M_w
USGS	global <i>W</i> phase	351°	16°	137°	213°	45.959° (<i>h</i>)	34.911° (<i>h</i>)	21.5 km (<i>c</i>)	1.12×10^{20} Nm	7.3
USGS	global body waves	33°	19°	178°	215°	45.959° (<i>h</i>)	34.911° (<i>h</i>)	19 km (<i>c</i>)	0.63×10^{20} Nm	7.1
GCMT	global waveforms	351°	11°	140°	210°	45.84° (<i>c</i>)	34.83° (<i>c</i>)	18 km (<i>c</i>)	1.6×10^{20} Nm	7.4
<i>This study</i>	teleseismic body waves, point source	7°	21°	157°	209°	N/A	N/A	23 km (<i>c</i>)	0.68×10^{20} Nm	7.2
<i>This study</i>	teleseismic body waves, line source	354° (<i>f</i>)	17°	142°	211°	N/A	N/A	17 km (<i>c</i>)	1.01×10^{20} Nm	7.3
<i>This study</i>	(acceptable ranges)		4–18°					15–18 km (<i>c</i>)		
<i>This study</i>	InSAR uniform slip (1σ uncertainties)	353.7° $\pm 0.5^\circ$	14.3° $\pm 0.4^\circ$	136.8° $\pm 0.8^\circ$	216°	45.863° (<i>u</i>) ± 100 m	34.738° (<i>u</i>) ± 150 m	14.8 km (<i>u</i>) ± 0.1 km	0.83×10^{20} Nm $\pm 0.01 \times 10^{20}$	7.2
<i>This study</i>	InSAR variable slip	353.7°	14.3°	136.8°	216°	45.863° (<i>u</i>)	34.738° (<i>u</i>)	14.8 km (<i>u</i>)	0.93×10^{20} Nm	7.25
Barnhart et al. (2018)	InSAR variable slip and rake	351°	15°	128.0° (<i>a</i>)	222°	45.87° (<i>p</i>)	34.65° (<i>p</i>)	15 km (<i>p</i>)	1.09×10^{20} Nm	7.3
Vajedian et al. (2018)	InSAR variable slip and rake	354.4°	17.5°	141.5° (<i>a</i>)	217°	45.864° (<i>p</i>)	34.675° (<i>p</i>)	16.9 km (<i>p</i>)	1.06×10^{20} Nm	7.3
Feng et al. (2018)	InSAR variable slip and rake	353.5°	14.5°	135.6° (<i>a</i>)	217°	45.866° (<i>u</i>)	34.734° (<i>u</i>)	14.5 km (<i>u</i>)	1.08×10^{20} Nm	7.3
Ding et al. (2018)	InSAR and teleseismic <i>P</i> waves	354.7°	16.3°	137.3°	212°	45.871° (<i>u</i>)	34.734° (<i>u</i>)	15.8 km (<i>c</i>)	1.10×10^{20} Nm	7.3
Chen et al. (2018)	InSAR and teleseismic <i>P</i> waves	351°	15°	135° (<i>a</i>)	215°	45.875° (<i>p</i>)	34.714° (<i>p</i>)	16.7 km (<i>p</i>)	1.35×10^{20} Nm	7.4

Note. SV is the slip vector of the hanging wall relative to the footwall. USGS = U.S. Geological Survey; GCMT = Global Centroid Moment Tensor Catalog. For our body waveform model, sensitivities in dip and centroid depth were determined by fixing these parameters at increments away from the minimum misfit value, solving for the remaining free parameters, and visually assessing the degradation in misfit. Uncertainties shown below our synthetic aperture radar interferometry (InSAR) uniform slip model are from Monte Carlo inversions of 100 synthetic data sets perturbed with realistic noise (supporting information Figure S2). Other parameters of our uniform slip model include slip 3.05 ± 0.04 m, top depth 12.2 ± 0.1 km, bottom depth 17.4 ± 0.2 km, length 40.1 ± 0.2 km, and width 21.2 ± 0.3 km. *c* = centroid location or depth; *h* = hypocenter location or depth; *u* = uniform slip model fault center point and depth; *p* = distributed slip model peak slip location and depth; *a* = average value across slip distribution; *f* = parameter fixed in inversion.

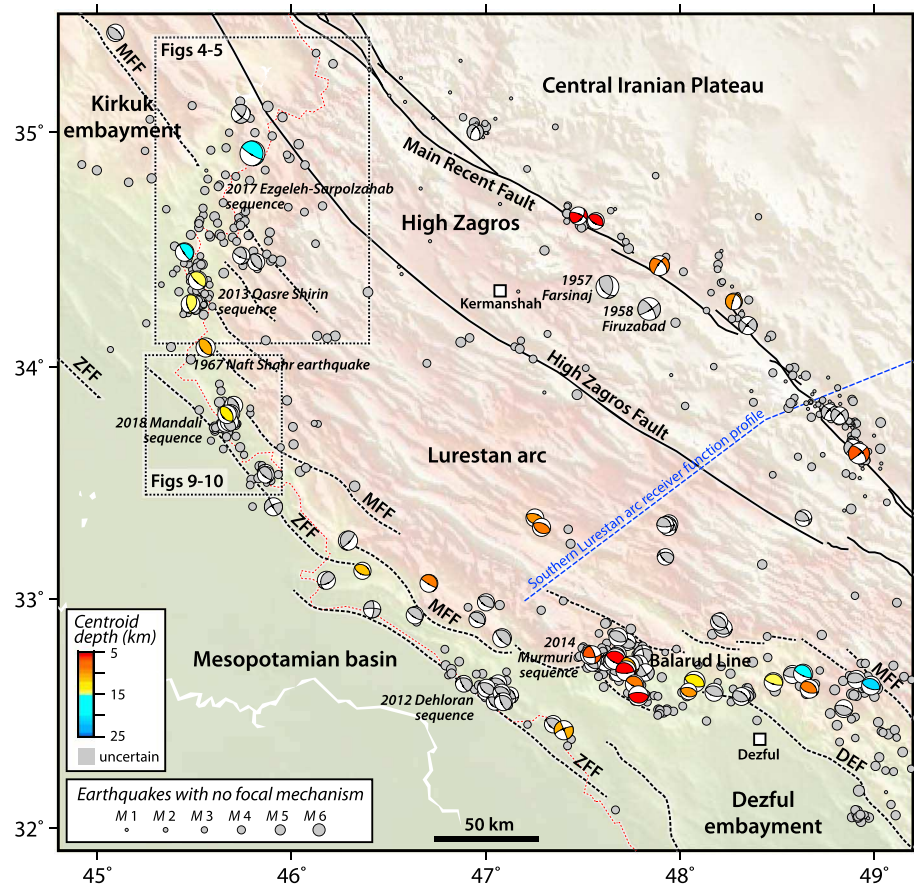


Figure 3. Earthquake epicenters, focal mechanisms, and mapped active faults in the Lurestan arc. All earthquakes are plotted at relocated epicentral locations from this study or that of Karasözen et al. (2017), except for the 1957 Farsinaj and 1958 Firuzabad earthquakes in the High Zagros, for which robust results with errors <6 km were not possible (though we suspect they do lie SW of the main trace of the Main Recent Fault). Focal mechanisms determined with teleseismic body waveform modeling are colored according to centroid depth. Black lines are faults; surface projections of Berberian's (1995) "master blind thrusts" are dashed (DEF = Dezful Embayment Fault; MFF = Mountain Front Fault; ZFF = Zagros Foredeep Fault). The blue line shows the trend of the receiver function profile of Paul et al. (2010) and Motaghi, Shabanian, and Kalvandi (2017).

The Lurestan arc is a ~ 300 km long, up to ~ 200 km-wide salient within the northwestern SFB, which averages $\sim 1,000$ – $1,500$ m in elevation, around a kilometer higher than the adjacent embayments (Figures 2a and 3). In this area, cessation of Neotethyan subduction beneath central Iran and onset of continental collision is dated between ~ 35 Ma (late Eocene) and ~ 25 Ma (late Oligocene; Agard et al., 2005), since when ~ 50 – 60 km of shortening has been accommodated (Blanc et al., 2003; McQuarrie, 2004). GPS velocities indicate ongoing northward directed convergence of $\sim 4 \pm 2$ mm/year between Arabia and central Iran at this longitude (Vernant et al., 2004). Although GPS data within the Lurestan arc are too sparse to resolve its internal kinematics, the overall N-S convergence is thought to be partitioned into roughly equal components of range-perpendicular shortening and range-parallel dextral shear, the latter focused along the Main Recent Fault in the High Zagros (Walpersdorf et al., 2006).

2.1. Geology

The stratigraphy of the Lurestan arc archives the geological history of the northeastern Arabian margin, from punctuated episodes of Paleozoic rifting culminating in the Mesozoic opening of the Neotethys ocean, to its eventual closure and the onset of continental collision with central Iran in the late Eocene (e.g., Alavi, 2004). Balanced cross sections depict cover thicknesses of ~ 6 – 10 km within the Lurestan arc (Blanc et al., 2003; Emami et al., 2010; Farzipour-Saein et al., 2009; Homke et al., 2009; McQuarrie, 2004; Sadeghi & Yassaghi, 2016; Vergés, Goodarzi, et al., 2011) and ~ 11 – 14 km in the Mesopotamian foreland SW of the arc (Blanc et al., 2003; Casciello et al., 2009; Emami et al., 2010; Farzipour-Saein et al., 2009; Sherkati et al., 2006;

Vergés, Goodarzi, et al., 2011). The difference is generally ascribed to vertical offset and exhumation across two major basement-cored reverse faults, the Zagros Foredeep Fault along the foreland deformation front, and behind it the Mountain Front Fault, which regionally marks the frontal outcrop of Oligocene-Miocene Asmari limestone (Berberian, 1995; Figure 2a). In contrast with the Fars arc, there is no firm evidence for basal Infracambrian Hormuz salt deposits in the northwestern SFB (Edgell, 1991; Kent, 1979). However, mechanical considerations point to an equivalent decoupling horizon in the Lurestan arc that allows the deformation front to advance southwestward over the Arabian plate (McQuarrie, 2004). Mesozoic strata of the Lurestan arc are also distinct, with fewer neritic limestones and more pelagic shales than in other parts of the Iranian Zagros (Casciello et al., 2009; Sepehr et al., 2006). There are three main detachment-forming horizons within the Lurestan cover sequence, each giving rise to folding of a distinctive wavelength (Casciello et al., 2009; Farzipour-Saein et al., 2009; Vergés, Goodarzi, et al., 2011). NW-SE trending surface anticlines form “whaleback” ridges expressed in resistant limestones of the Cretaceous Bangestan group and the Oligocene-Miocene Shahbazan-Asmari formations, while synclines typically expose Miocene-Pliocene Gachsaran evaporites and Agha Jari and Bakhtyari sandstones and conglomerates.

2.2. Crustal Structure

The deep crustal structure of the Lurestan arc also differs significantly from other parts of the Zagros. The depth to the magnetic basement from spectral analysis of aeromagnetic data is ~ 16 km, greatly exceeding stratigraphic estimates and thus implying that uppermost crystalline rocks are only weakly magnetized, perhaps due to deformation and alteration (Teknik & Ghods, 2017). A receiver function profile across the southern Lurestan arc (location shown in Figure 3) reveals a horizontal (in section) interface at ~ 17 km depth, the like of which is absent from a parallel profile across the Fars arc (Motaghi, Shabanian & Kalvandi 2017; Motaghi, Shabanian, Tatar, et al., 2017). This structure is interpreted as a basement décollement which transports overriding rocks toward the SW deformation front of the arc. Although Lurestan and Fars arc receiver function profiles indicate similar average Moho depths of ~ 45 km (Paul et al., 2010), L_g waves propagate more efficiently across the Lurestan arc than other parts of the Iranian Zagros, implying smoother lateral variations in crustal thickness (Maheri-Peyrov et al., 2016).

2.3. Seismicity

Before 2017, the largest instrumentally recorded earthquakes in the Lurestan arc were $M_w \sim 6$; the historical record shows one magnitude ~ 6.4 earthquake around 1000 CE in the Sarpolzahab region (Ambraseys & Melville, 1982; Berberian, 1995). Seismicity is strongly focused around the edges of the arc, in yet another contrast with Fars where earthquakes are spread more diffusely across a width of ~ 100 – 200 km (Figure 2a). Many of the larger Lurestan events also cluster in time, forming energetic swarms or aftershock sequences such as at Dehloran in 2012 (Nippres et al., 2017), Qasr Shirin in 2013 (this study), and Murmuri in 2014 (Copley et al., 2015; Motagh et al., 2015; Figure 3). There is a predominance of thrust mechanisms with gentle ($\sim 20^\circ$) to moderate ($\sim 45^\circ$) fault planes, and the absence of subhorizontal ($< 10^\circ$) nodal planes has been used to argue against a regional seismic décollement (Nissen et al., 2011; Talebian & Jackson, 2004). Many of the larger events studied with teleseismic waveforms (Maggi et al., 2000; Nissen et al., 2011; Talebian & Jackson, 2004) and/or InSAR (Copley et al., 2015; Motagh et al., 2015) have shallow, ~ 3 – 7 km centroid depths consistent with rupture of the lower sedimentary cover, though two earthquakes at the edge of the Dezful embayment with ~ 17 – 20 km centroid depths (Maggi et al., 2000) are unequivocally basement events. To date, no earthquakes in the Kirkuk embayment have been analyzed with these same methods, but regional moment tensor solutions for a few $M \sim 4$ – 5 Kirkuk events have centroid depths of ~ 13 – 25 km, also consistent with basement activity (Abdulnaby et al., 2014).

2.4. Structural Relations With the Dezful and Kirkuk Embayments

The seismicity distribution prompts a close inspection of the structural relations between the Lurestan arc and the adjacent embayments. To the south, the sedimentary cover of the Dezful embayment is substantially thicker (at 12 ± 3 km) and the stratigraphic exposure level higher than in Lurestan (Abdollahie-Fard et al., 2006; Ahmadi et al., 2007; Blanc et al., 2003; Carruba et al., 2006; Derikvand et al., 2018; Sherkati & Letouzey, 2004; Sherkati et al., 2006), with the difference accommodated by a structural step or flexure known as the Balarud line (Figure 2a). The E-W orientation of the Balarud line is unusual for the Zagros, where most basement and cover structures trend approximately NW-SE or approximately N-S. It truncates and sometimes deflects but does not actually offset NW-SE trending folds on either side of it, as if the abrupt contrast in stratigraphy prevents folds from propagating across it (Allen & Talebian, 2011). Although it is sometimes depicted as a sinistral strike-slip fault (e.g., Hessami et al., 2001; Sepehr & Cosgrove, 2004), there

is no evidence from surface geology or seismicity of a continuous fault along the Balarud line (Allen & Talebian, 2011); instead, focal mechanisms and epicenters seem to support an en echelon arrangement of W-to-NW striking reverse or oblique-reverse faults.

To the north, basement depths within the Kirkuk embayment are relatively poorly constrained but may be somewhat greater than in Lurestan at 10 ± 2 km (Bretis et al., 2011; de Vera et al., 2009; Hinsch & Bretis, 2015; Koshnaw et al., 2017; Obaid & Allen, 2017; Sadeghi & Yassaghi, 2016). However, the Kirkuk embayment exposes younger rocks than in adjacent parts of the Lurestan arc and fold axes are truncated along the boundary, consistent with a deep-seated structural divide. Berberian (1995) interprets this boundary as an en echelon set of right stepping, approximately NW striking segments of the Mountain Front Fault (the arrangement plotted on Figure 2a). In contrast, Hessami et al. (2001) and Bahroudi and Talbot (2003) depict the boundary as a single, throughgoing right-lateral fault, termed the Khanaqin fault, which follows the same approximately N-S structural trend as lineaments mapped in the central Arabian plate. The 2013 Qasre Shirin, 2017 Ezgeleh-Sarpolzahab, and 2018 Mandali sequences studied in this paper are among the first large events along this trend and will thus provide important new constraints on its kinematics.

3. Data and Methods

3.1. Hypocentral Distribution From Calibrated Earthquake Relocations

We determined the distribution of hypocenters in the Ezgeleh-Sarpolzahab region using the hypocentroidal decomposition algorithm (Jordan & Sverdrup, 1981) implemented within the *Mloc* multiple-earthquake relocation program (Bergman & Solomon, 1990). This obtains absolute, calibrated event hypocenters and origin times (with uncertainties) of clusters of earthquakes from large arrival time data sets by reducing bias from unknown Earth velocity structure. The relocation is divided into two independent inverse problems with data tailored to each step. First, it solves for the cluster vectors that connect each event hypocenter to the hypocentroid—defined as the geometric mean of all hypocenters—using all available data at any epicentral distance. Second, it calculates the absolute location of the hypocentroid and updates the absolute hypocenter coordinate of every event in the cluster, using either phase picks at close-in stations that record direct P_g and S_g arrivals (termed *direct calibration*), or ground truth locations of one or more events in the cluster determined by independent means (*indirect calibration*; e.g., Ghods et al., 2012, 2015; Karasözen et al., 2016, 2018; Walker et al., 2011).

Our cluster contains the mainshock, ~110 well-recorded early aftershocks up to 1 April 2018, and ~140 preceding earthquakes including ~40 events of the 2013 Qasre Shirin sequence. A concentration of ~20 aftershocks in mid-January 2018 near the Iraqi border town of Mandali are included (~80 km south of Sarpolzahab); three notable late aftershocks (M_w 5.8, 6.0 and 6.3 earthquakes on 22 July, 25 August, and 25 November 2018) are excluded but will be the subject of a follow-up study. Most events are larger than m_b/M_L 3.0, though a few smaller earthquakes or events of unassigned magnitude are also included. Arrival time data were assembled from the International Seismological Centre, the USGS National Earthquake Information Center, the Iranian National Seismograph Network, the Iranian Building and Housing Research Network (BHRC), the Iranian Seismological Center (IRSC), the Iraqi Broadband Seismic Network, the Iraqi Seismic Observatory, the Kurdistan Seismic Network, and the Jordan Seismic Network. We also exploited two temporary seismometers installed near Sarpolzahab after the 2017 mainshock, as well as stations of the China-Iran Geological Geophysical Survey in the Iranian Plateau, a larger temporary network in operation from October 2013 to October 2014 (Chen et al., 2016), which proved useful for relocating the November 2013 Qasre Shirin earthquakes.

The regional station coverage (Figure 1b) is much better east of the earthquake than west of it, so a direct calibration could be prone to significant biases in longitude which would be hard to detect. Therefore, we used indirect calibration as a way of providing additional confidence in the reliability of our direct calibration results. We chose 16 calibration events from 2013 to 2014 recorded at common stations with the 2017 Ezgeleh-Sarpolzahab sequence as well as at Baghdad (BHD) and Kirkuk (IKRK) to the west (Figure 1b and supporting information Table S1). We relocated these 16 events separately using direct calibration and then used these results to relocate other earthquakes in the cluster in an indirect calibration. We develop a custom 1-D crustal velocity model by fitting P_g , S_g , P_n , and S_n arrival times, with V_p 5.75 km/s and V_s 3.25 km/s for the top 12 km and V_p 6.15 km/s and V_s 3.5 km/s from 12 km to the Moho at 47 km. These velocities are broadly consistent with those obtained from Zagros microseismic studies, as summarized in Nissen et al. (2011, 2014). Final 90% confidence limits on epicentral (horizontal) location vary between ~2.0 and ~5.5 km.

Focal depths are set manually by minimizing residuals at nearby stations for each event; by observing how residuals vary across a spread of fixed depths, we estimate typical uncertainties of ≤ 4 km in our preferred values. This marks a significant improvement over errors of ~ 10 km or larger in catalogue focal depths in the Iran region (Maggi et al., 2002; Engdahl et al., 2006).

3.2. Focal Mechanisms From First Motions and Waveform Modeling

We used P wave first motion polarities and long-period P and SH waveform modeling to compute focal mechanisms for the nine of the largest earthquakes in the 2017 Ezgeleh-Sarpolzahab sequence, the mainshock of the January 2018 Mandali sequence, and the three largest earthquakes of the November 2013 Qasre Shirin sequence. Where available, we compare these results with automated solutions produced by the USGS National Earthquake Information Center and the GCMT project.

First motion polarities were used to compute best double-couple focal mechanisms of the 12 November 2017 $M_L \sim 4$ foreshock and seven $M_L \sim 4$ –5.5 aftershocks. We used regional broadband seismograms of the IRSC, the Iranian National Seismograph Network, and the Iraqi Broadband Seismic Network, as well as two of our own stations deployed near Sarpolzahab (Figure 1b). As is commonly observed for Zagros earthquakes, P waves were generally emergent, making picking first motion polarities challenging for smaller events with low signal-to-noise ratios. This was especially the case for BHRC accelerometers and IRSC short-period instruments, whose 12-bit digitizers and 1-Hz corner frequencies were unable to capture the very emergent part of the waveform, and for this reason we avoided picking polarities for these stations. Nevertheless, the accelerometers record some interesting directivity effects, which we discuss in section 4.

Separately, we used long-period teleseismic body waves to determine source parameters and centroid depths for the M_w 7.3 Ezgeleh-Sarpolzahab mainshock, the M_w 5.5 Mandali mainshock, and the three largest M_w 5.6–5.8 Qasre Shirin earthquakes. At periods of 15–100 s and distances of 30–80°, body waveforms are insensitive to short-wavelength heterogeneities in local velocity structure and fault slip, such that earthquakes in the magnitude range $M_w \sim 5$ –7 generally appear as simple point sources (e.g., Molnar & Lyon-Caen, 1989). The shape, amplitude, and relative timing of direct P and SH waves and their near-source surface reflections pP , sP , and sS can be used to determine a moment tensor or best double couple solution for a simple point or line source, including a centroid depth to a typical ± 3 km uncertainty (Maggi et al., 2000; Molnar & Lyon-Caen, 1989; Nissen et al., 2014; Taymaz et al., 1991). Though this methodology provides more robust centroid depths than the automated solutions of the USGS and GCMT catalogs, it is also known to underestimate seismic moments by a factor of up to 2 compared to solutions derived from longer period waveforms (e.g., USGS W phase, GCMT); we consider the latter to be the better estimates of magnitude (Molnar & Lyon-Caen, 1989).

Each event was analyzed using around 50 Global Digital Seismic Network seismograms across the distance range 30–80°, selected on the basis of signal-to-noise and azimuthal coverage. We applied a 15–100 s band-pass filter and modeled P waveforms on vertical component seismograms and SH waveforms on transverse seismograms. We used the algorithm of McCaffrey and Abers (1988) and McCaffrey et al. (1991) within the MT5 software of Zwick et al. (1994) to minimize the sum of squared residuals between observed waveforms and synthetic seismograms calculated for a point or line source embedded within an elastic half-space with $V_p = 5.9$ km/s, $V_s = 3.4$ km/s and density $\rho = 2700$ kg/m³ (consistent with the average upper crustal velocities determined by hypocentral relocations). We computed best double-couple solutions by solving for the strike, dip, rake, centroid depth, and a source time function comprising a series of overlapping isosceles triangles of duration 1 s. Synthetic seismograms were generated from P , pP , and sP phases (vertical component) and S and sS phases (transverse component), with the direct phases first aligned using the broadband records, thus eliminating any errors from centroid mislocation. Waveform amplitudes were corrected for geometrical spreading (Langston & Helmberger, 1975) and for anelastic attenuation, using a ratio of travel time to average Q of 1 s for P waves and 4 s for SH waves (Futterman, 1962). Seismograms were weighted according to azimuthal density such that closely spaced stations are not given undue influence (McCaffrey & Abers, 1988; Zwick et al., 1994) with SH weights further halved to compensate for their larger amplitudes. Finally, the sensitivities of the key parameters of dip and centroid depth within the inversion were assessed by fixing them at increments away from the minimum misfit value, solving for the remaining free parameters, and visually assessing the degradation in fit between synthetic and observed waveform (Molnar & Lyon-Caen, 1989; Taymaz et al., 1991).

3.3. Fault Geometry and Slip Distribution From InSAR

We used InSAR imagery from the European Space Agency Sentinel 1A and 1B satellites to assess the geometry and slip distribution of the M_w 7.3 12 November 2017 Ezgeleh-Sarpolzahab mainshock. We constructed four interferograms from two adjacent ascending orbital tracks (072A and 174A) and two descending ones (006D and 079D), each encompassing between 5 and 7 days of postseismic deformation (Figure 1b). We also assessed the Mandali earthquakes of 11 January 2018, which include three M_w 5.2–5.3 aftershocks in the hour following the M_w 5.5 mainshock. Here, we constructed two Sentinel interferograms from ascending track 072A and descending track 006D that include six days of postseismic deformation and 1 day of postseismic deformation, respectively. For the latter pair of interferograms, we also enhanced the relatively subtle tectonic signal by applying a linear correction for topographically correlated atmospheric water vapor (Elliott et al., 2008).

To characterize the faulting responsible for the observed surface displacements, we employed a standardized elastic dislocation modeling procedure (e.g., Elliott et al., 2012; Wright et al., 1999). The wrapped interferograms were first downsampled using a quadtree algorithm that concentrates sampling in areas with steep phase gradients (Jónsson et al., 2002). Each sampled data point comprises easting and northing coordinates, the local (as opposed to a fixed) line-of-sight unit vector, and the displacement along that line-of-sight. We inverted the reduced data using Powell's algorithm (Press et al., 1992), avoiding local minima by repeating the inversion 1,000 times with starting parameters sampled randomly from within the ranges given in the captions to supporting information Figures S2 and S10 and retaining only the lowest minimum solution (Clarke et al., 1997; Wright et al., 1999). We solved for the optimal strike, dip, rake, length, top and bottom depths, and uniform slip, for a rectangular fault plane embedded within an elastic half space (Okada, 1985) with Lamé parameters $\mu = \lambda = 3.2 \times 10^{10}$ Pa and Poisson ratio 0.25, consistent with upper crustal seismic velocities estimated from calibrated earthquake relocations and used in the body waveform modeling. To account for uncertainties in satellite orbital parameters, we also jointly solved for linear N-S and E-W orbital ramps and ambiguities in zero displacement. Uncertainties in source parameters were established by applying the same uniform slip inversion procedure to 100 synthetic data sets perturbed with correlated noise characterized from undeformed parts of each interferogram (Funning et al., 2005). This Monte Carlo approach gives rise to Gaussian distributions in each individual source parameter, from which standard deviations can be drawn, and also helps to illustrate important trade-offs between certain parameters.

Having established the fault geometry, the model fault was subdivided into smaller 3×3 km patches and the slip distribution estimated using a Laplacian operator to force realistic smoothing (Wright et al., 2003). For the Ezgeleh-Sarpolzahab mainshock, we tested variable rake models but found minimal visual improvement over the uniform rake model, which we prefer for its smaller number of free parameters. For the Mandali earthquakes, we found a strong trade-off between slip magnitude and fault width (e.g., Nissen et al., 2010; Roustaei et al., 2010) that makes the detailed slip distribution difficult to resolve and so we present only the uniform slip model, with slip fixed at 0.5 m in the inversion.

We also compared our results with Barnhart et al.'s (2018) model for the Ezgeleh-Sarpolzahab mainshock, based on exactly the same InSAR data and assumed Earth elasticity but different approaches to data sampling and model regularization. This comparison helps us to assess what is robust in each model. Barnhart et al. (2018) explored a population of 460 different fault geometries which varied incrementally in strike, dip, and depth. They inverted the downsampled Sentinel-1 interferograms for the distribution of slip on each plane using triangular elastic Green's functions (Meade, 2007) and an iterative fault discretization approach that resizes the fault slip patches such that the size of a patch reflects the resolution capability of the model in that location (Barnhart & Lohman, 2010). The inversions were regularized with a minimum moment constraint that is length-scale independent. The inversions allowed for variable slip direction in the thrust direction (both dextral and sinistral slip allowed), and a subpopulation of "best fit" models (those which minimize the degree to which noise is mapped into slip) were analyzed based on model fits defined by the J_R criterion (Barnhart & Lohman, 2010; Nealy, Benz, et al., 2017).

3.4. Mainshock Rupture Progression From Finite Fault Modeling and Backprojection

We mapped the rupture progression of the 12 November 2017 Ezgeleh-Sarpolzahab mainshock using two complementary but independent methods. The first method maps slip evolution onto an imposed fault plane geometry by inverting teleseismic P , SH , and long-period surface waveforms (Ji et al., 2002; Hayes, 2017). The

Table 2*Other Earthquake Focal Mechanisms Determined Using First Motions in the Ezgeleh-Sarpolzahab Sequence*

Date	Time	Strike	Dip	Rake	Strike	Dip	Rake	Longitude	Latitude	Focal depth	M_L
12.11.2017	17:35	345°	7°	135°	120°	85°	85°	45.810°	34.892°	17 km	~4
12.11.2017	22:31	341°	36°	73°	182°	56°	102°	45.604°	34.642°	13 km	~4.5
12.11.2017	23:37	227°	64°	16°	130°	76°	153°	46.067°	34.661°	7 km	~4
13.11.2017	13:12	262°	54°	19°	161°	75°	142°	45.804°	34.493°	15 km	~4
18.11.2017	04:12	346°	33°	62°	198°	61°	107°	45.582°	34.557°	14 km	~4
11.12.2017	14:09	128°	78°	27°	32°	64°	167°	45.739°	35.078°	14 km	~5.5
11.12.2017	14:42	330°	73°	-10°	63°	80°	-163°	45.766°	35.084°	15 km	~4
20.12.2017	20:22	72°	82°	6°	341°	84°	172°	46.160°	34.687°	5 km	~4.5

Note. Time is in Coordinated Universal Time and longitude and latitude refer to the epicenter. Date is formatted as DD.MM.YYYY.

second method back projects P waveforms to track the source of high frequency seismic energy horizontally, making no assumption about fault geometry or mechanism (Ishii et al., 2005; Zhang & Ge, 2010).

For the finite fault modeling, we selected 46 teleseismic broadband P waveforms, 21 broadband SH waveforms, and 72 long period surface waveforms based on data quality and azimuthal distribution (Hayes, 2017) and incorporated velocity records in addition to displacement seismograms in order to improve resolution (Nealy, Herman, et al., 2017). We assumed the fault geometry derived from InSAR modeling, subdivided it into rectangular cells with length 3.0 km and width 3.5 km, and solved for the rupture initiation time, source time function, slip amplitude, and slip vector of each cell using the wavelet transform approach of Ji et al. (2002). The source time function is approximated as an asymmetric cosine characterized by “starting-phase” and “ending-phase” times (Ji et al., 2003). We forced the slip to initiate near the hypocenter as determined in section 3.1 and constrained the rupture velocity to the range 1.5–3.5 km/s. We also assessed the sensitivity of the slip model to starting focal depth and fault dip, by perturbing and fixing these parameters at increments away from the preferred model, solving again for the slip distribution, and assessing the model-data waveform misfits visually.

For the backprojection, we used 47 seismograms from stations in Asia and Australia within the distance range 40–90°, each exceeding a threshold coefficient of 0.85 in the coherence of the early part of the P waveform (supporting information Figure S1). These were cleaned using a 0.2–2 Hz band-pass filter. We defined a grid surrounding the mainshock epicenter and calculated theoretical traveltimes between each grid node and each station using an assumed source depth of 15 km. We used the phase weighted stacking method of Schimmel and Paulssen (1997) and backprojected the energy emitted at 1-s intervals using an 8-s stacking window onto a grid surrounding the mainshock epicenter.

4. Results

4.1. The 12 November 2017 Ezgeleh-Sarpolzahab Mainshock

The mainshock initiated a few kilometers north of Ezgeleh, on the Iran-Iraq border (Figure 4). Relatively large ($\pm \sim 1$ s) travel time residuals at the closest stations (KSBB at 0.17° epicentral distance and KSDD at 0.23°; Figure 1b) prevent a very precise determination of focal depth, and we estimate an uncertainty of ~ 4 km in our preferred solution of ~ 19 km. The mainshock hypocenter is almost exactly collocated with the $M_L \sim 4$ (m_b 4.2, International Seismological Centre) foreshock that occurred ~ 43 min beforehand, with a similar focal mechanism and focal depth (Table 2).

South of the mainshock epicenter, ascending and descending interferograms both display an elongate, approximately N-S oriented, elliptical pattern of surface displacements toward the satellite, with peak line-of-sight values of ~ 90 and ~ 60 cm, respectively (Figures 5a–5d). In the descending interferograms, a second broad fringe ellipse east of the epicenter contains displacements of up to ~ 45 cm away from the satellite. Our initial uniform slip elastic dislocation model reproduces these patterns with ~ 3 m of oblique (reverse right lateral), SW directed slip on a ~ 40 km-long, ~ 21 km-wide, $\sim 14^\circ$ east dipping fault, between depths of ~ 12 and ~ 18 km (Table 1, line 7). Monte Carlo inversions of data sets perturbed with realistic noise (supporting information Figure S2) show that the solution is tightly constrained, presumably by the large signal-to-noise ratio and four independent look directions, with the caveat that all of these results were

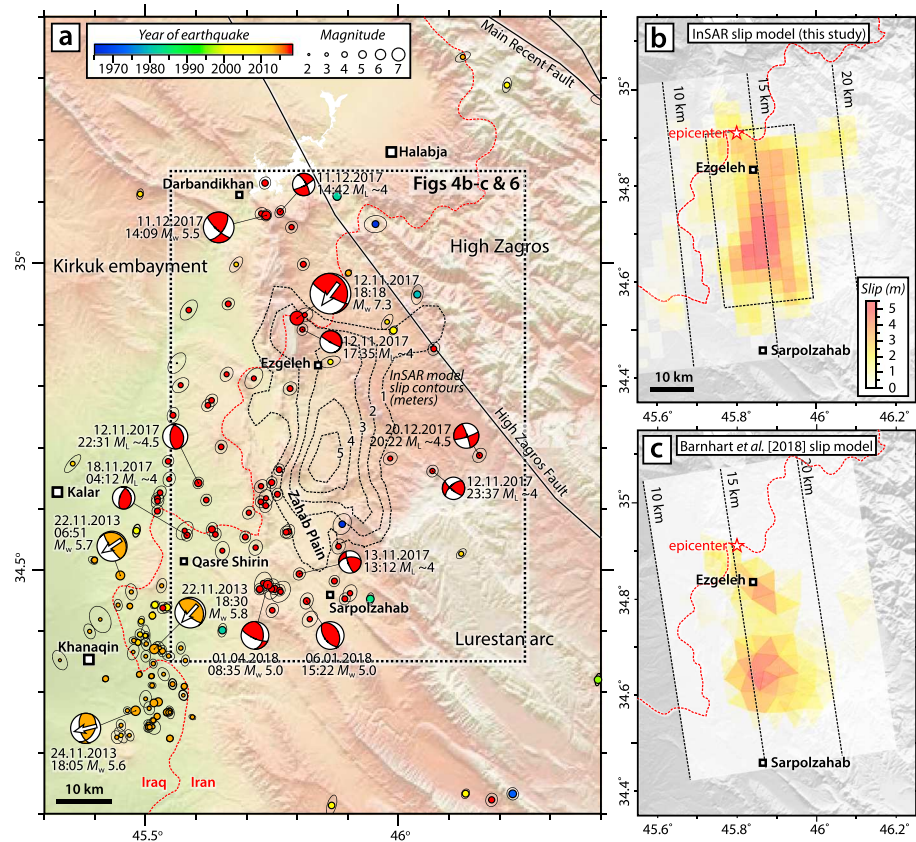


Figure 4. (a) Earthquakes in the northwestern Lurestan arc, plotted at relocated epicentral locations with 90% confidence ellipses. Epicenters (circles) and available focal mechanisms are colored by time, with the 2013 Qasre Shirin sequence in orange and the 2017 Ezgeleh-Sarpolzahab sequence in red. Mechanisms for the four largest events (each $M_w \geq 5.6$) are from our own body waveform modeling, and here we also plot the slip vector. Mechanisms for the intermediate events (M_w 5.0–5.5) are from the U.S. Geologic Survey *W* phase or Global Centroid Moment Tensor catalogs, and those for the smallest events (M_L 4–4.5) are from our own first motions analyses. Dashed black lines show contours (in meters) of our InSAR slip model. (b) Colors show coseismic slip in the 12 November 2017 Ezgeleh-Sarpolzahab mainshock from elastic dislocation modeling of the four interferograms in Figures 5a–5d. Dashed lines show 10 km, 15 km and 20 km contours of the model fault plane. (c) Coseismic slip distribution and model fault plane contours for the InSAR-derived model of Barnhart et al. (2018). InSAR = synthetic aperture radar interferometry.

obtained under assumptions of uniform slip on single rectangular fault planes. We estimate an average stress drop of ~ 2.7 – 3.7 MPa using the equations of Kanamori and Anderson (1975) for rectangular strike-slip and dip-slip faults, close to the middle of the range observed worldwide (Allmann & Shearer, 2009). The variable slip model further improves the fit to the observed interferograms (Figures 5e–5h), with line-of-sight displacement residuals mostly below ± 10 cm (Figures 5i–5l). Here, slip spreads outside the bounds of the uniform slip plane, but $\sim 95\%$ of the seismic moment still occurs between depths of 10 and 20 km (Figure 4b). The epicenter lies at the northern edge of the slip area, indicating a strong southward directivity.

Our model is broadly consistent with other recent InSAR-derived slip models for this earthquake, which collectively agree to within $\sim 4^\circ$ in strike, $\sim 3^\circ$ in dip, $\sim 13^\circ$ in rake, and ~ 2 km in the fault center or peak slip depth (Barnhart et al., 2018; Chen et al., 2018; Ding et al., 2018; Feng et al., 2018; Vajedian et al., 2018; Table 1, lines 10–14). In Figure 4c, we compare our own slip distribution with the earliest of these alternative models, that of Barnhart et al. (2018). Both models support peak slip of 5–6 m at ~ 15 km depth in the southern part of the rupture area, about two thirds of the rupture length along strike from the epicenter, but small slip patches that lie near the up-dip or down-dip limits of the model fault planes are likely artifacts since none are common to both models. Crucially, the top and bottom edges of the main slip area are well resolved and in close agreement. Given sedimentary cover thicknesses of ~ 8 km in the Lurestan arc (section 2.1), the Ezgeleh-Sarpolzahab mainshock probably ruptured entirely within the basement. InSAR model moments

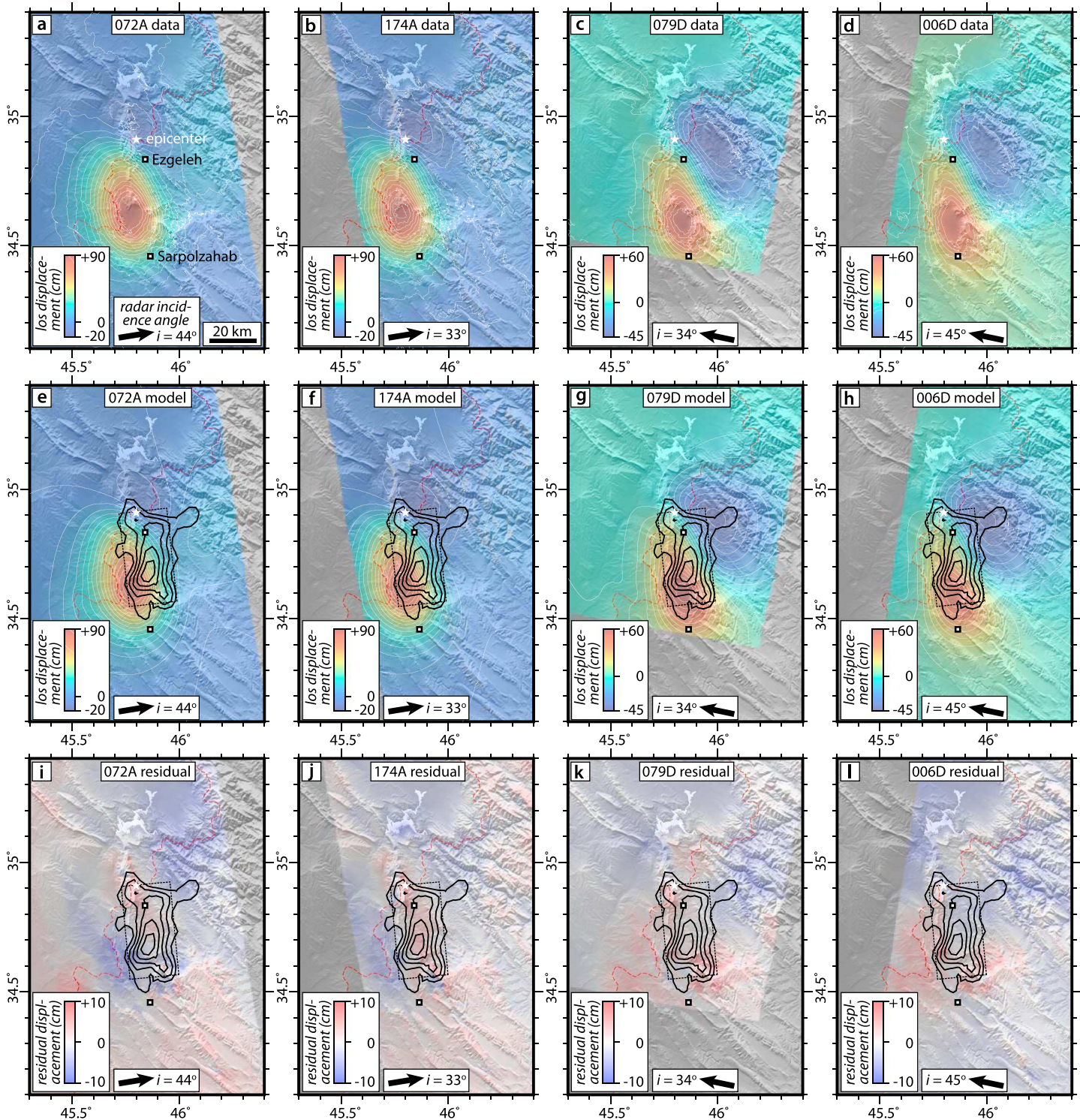


Figure 5. The top row of panels shows unwrapped coseismic interferograms from (a) ascending track 072 (11–17 November 2017), (b) ascending track 174 (6–18 November 2017), (c) descending track 079 (12–18 November 2017), and (d) descending track 006 (7–19 November 2017). Large black arrows show the radar incidence angle in the epicentral region (with i its inclination from the vertical). White lines show 5-cm line-of-sight displacement contours; positive displacements are toward the satellite and thus in the opposite sense to the radar incidence angle. The middle row (e–h) shows the equivalent model interferograms, with 1-m slip contours in black. The thin dashed rectangle marks the bounds of the uniform slip plane. The bottom row (i–l) shows the equivalent residual interferograms (model minus data).

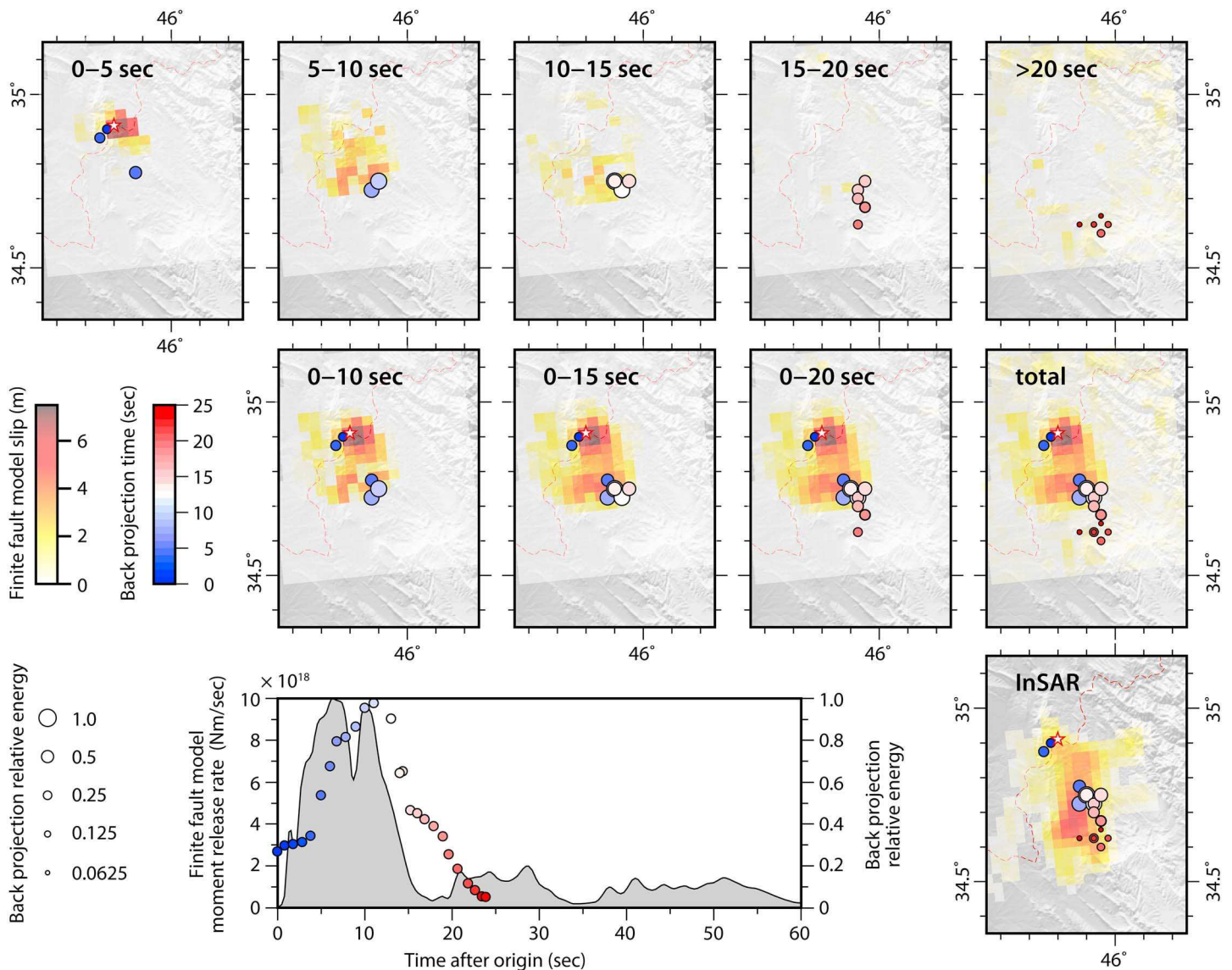


Figure 6. Finite fault model and back projection of the 12 November 2017 Ezgeleh-Sarpolzahab mainshock. The top row of panels shows 5-s increments of finite fault model slip (background color) and backprojection energy release (circles, scaled by relative energy and colored by time). The star in the first panel is the relocated mainshock hypocenter. The second row of panels shows the corresponding *cumulative* slip and energy release. The lower right panel shows the slip distribution from our InSAR slip model (Figure 4b) for comparison. The lower middle graph shows the moment release rate of the finite fault model (gray) and the energy history of the back projection (colored circles).

of $\sim 0.9\text{--}1.1 \times 10^{20}$ Nm lie within the range of seismological estimates ($\sim 0.6\text{--}1.6 \times 10^{20}$ Nm), indicating that the deformation captured in the interferograms is mostly related to seismic slip.

The strong southward rupture directivity apparent from comparing the calibrated epicenter with the InSAR slip distribution (Figures 4–5) is independently confirmed by our finite fault modeling and backprojection results (Figure 6 and supporting information Figures S3 and S4). Both methods seem to indicate two distinct parts to the earthquake, giving rise to separate peaks in seismic slip and energy release; the first from 0 to ~ 5 s close to the epicenter, and the second from ~ 5 to ~ 25 s to the south. This contrasts somewhat with the smoother InSAR slip distribution, which contains a single clear peak in slip, in the vicinity of the southern seismological slip asperity; likely, there is some segmentation to the rupture plane that is below the resolution of the InSAR modeling.

The backprojection results suggest that the rupture proceeds at $\sim 2\text{--}3$ km/s over the first 5–10 s, before slowing to $\sim 1\text{--}1.5$ km/s for the remainder of the earthquake, terminating after ~ 24 s ~ 35 km SSE of the epicenter.

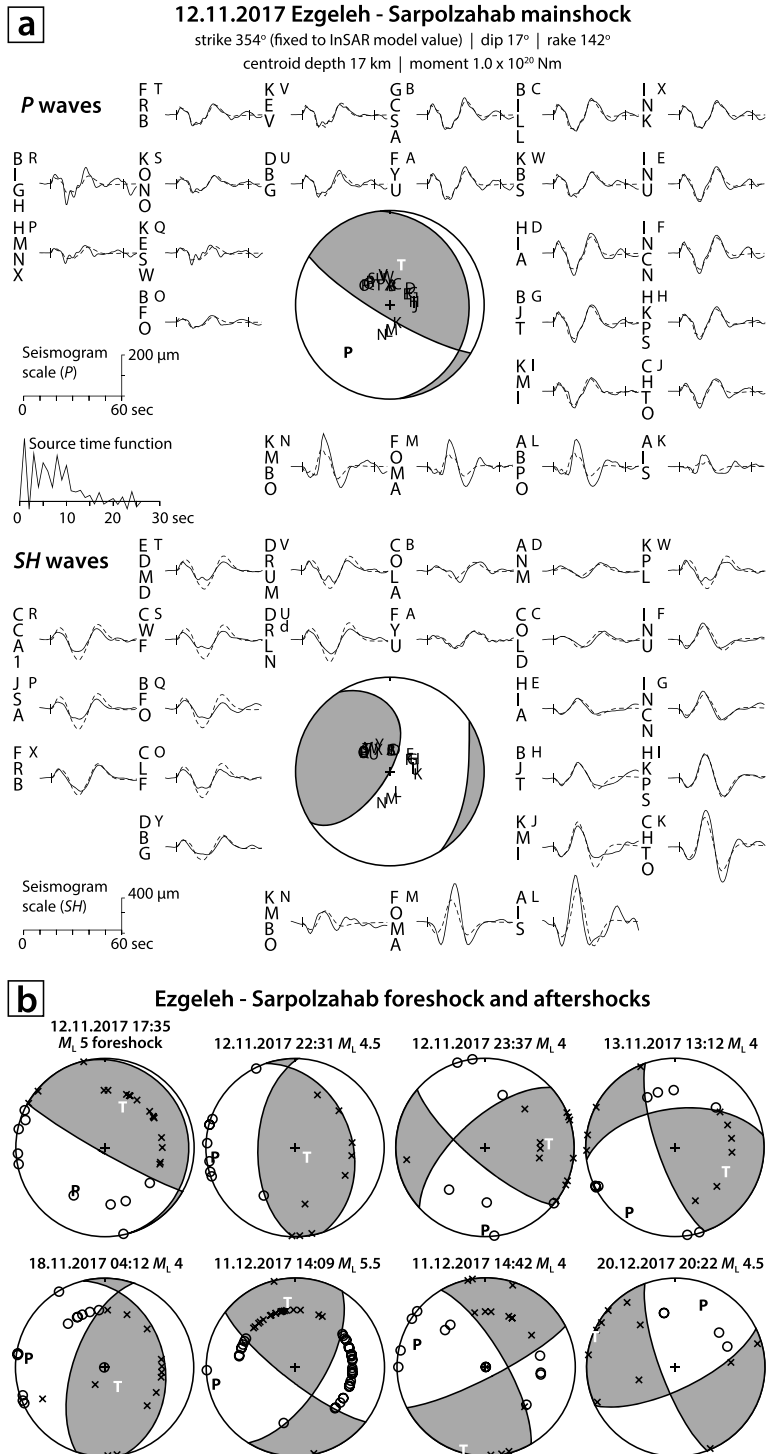


Figure 7. (a) Line source teleseismic body waveform model of the 12 November 2017 Ezgeleh-Sarpolzahab mainshock. The upper part shows the *P* focal sphere with nodal planes (lines), station positions (capital letters), and *P* and *T* axes (bold *P* and *T*), surrounded by observed (solid) and synthetic (dashed) seismograms, with station codes written vertically next to the focal sphere station position letter. Vertical ticks mark the *P* arrival time and the 45-s inversion window end. The lower part shows the *SH* focal sphere and seismograms; the inversion window is 60 s. The source time function and a time scale bar for the seismograms are shown on the left of the figure. Seismogram amplitudes are corrected for a distance of 40°. (b) Focal mechanisms from first motion polarities for the foreshock and seven aftershocks. InSAR = synthetic aperture radar interferometry.

Rupture in the finite fault model averages ~ 2 km/s for the first 10–15 s, accounting for most of the seismic moment release; after ~ 15 s the rupture is less well resolved. The long tail to the source time function (>25 s) involves slip well outside the limits of the InSAR slip distribution and is thus likely an artifact of late noise and the variable rupture velocity permitted in the inversion procedure (i.e., at the edges of the model space, the rupture velocity is artificially low and noise is mapped into slip). An average rupture velocity of ~ 1.5 – 2.0 km/s places the Ezgeleh-Sarpolzahab earthquake toward the lower limit of values observed for large earthquakes globally (Chounet et al., 2018).

Source geometries of the USGS *W* phase solution, the GCMT catalog mechanism, and our InSAR model are consistent to within a few (3–6) degrees in strike, dip and rake (Table 1). In contrast, parameters derived from teleseismic body waves—including a second USGS solution and our own point source model—are distinct, with a \sim NNE oriented strike, a steeper $\sim 20^\circ$ dip, and a larger component of right-lateral slip than the other solutions (Table 1, lines 2 and 4). However, our own point source body waveform model matches observations poorly, particularly for *SH* seismograms at northern and southern azimuths (supporting information Figure S5). Imposing a line source with a southward directivity (parameterized by fixing the strike to that of our InSAR model) gave a much improved fit to these stations and produced minimum misfit values of dip ($\sim 17^\circ$) and centroid depth (~ 17 km) much closer to those obtained with InSAR (Figure 7 and Table 1, line 5). Our preferred solution is for a line source with velocity 2.0 km/s, though there is little degradation to the waveform fits at faster rupture speeds. The source time function has a duration of 20–25 s, consistent with the back projection results, with most of the seismic moment released in the first 10–15 s, consistent with both the back projection and finite fault model. Though the line source model is still overly simplistic, it is the only one of our seismological methods that solves explicitly for centroid depth and so serves as an important, independent verification of the depth extents of the InSAR model fault. Altering and fixing the line source centroid depth within the bounds of 15–18 km makes little discernable difference to the waveform misfits, but the dip is relatively poorly constrained, with an acceptable range of 4 – 18° (Table 1, line 6). Similar tests undertaken for our finite fault model provide tighter constraints on fault dip of 10 – 16° , but rather limited constraints on focal depth with good fits across the range ~ 13 – 22 km (supporting information Figure S6).

The rupture history and directivity determined with teleseismic waveforms are also consistent with strong motion records observed locally (Figures 8a and 8b). Ground accelerations are skewed toward the south of the rupture with the largest (698 cm/s², or ~ 0.7 g) recorded at Sarpolzahab (BHRC station SPZ), ~ 45 km south of the epicenter and ~ 5 – 10 km south of the rupture termination (Figure 8c). SPZ is located in the northern part of Sarpolzahab, which was only lightly damaged compared to other parts of the city, and according to the BHRC has a moderate average shear wave velocity of the upper 30 m (V_s^{30}) of 619 m/s. Accordingly, the accelerations recorded at SPZ do not appear to be enhanced by site effects. The BHRC station at Ezgeleh was only installed after the mainshock and so the closest recording north of the rupture is at Nowsud (NSD), ~ 45 km NE of the epicenter, where peak ground acceleration is just 55 cm/s² (Figure 8d). The BHRC station GRS, which is a similar distance south of the rupture area as NSD is north of it, recorded a peak ground acceleration of 309 cm/s². All of the closest accelerograms show two packets of *S* waves indicative of the two distinct stages of the rupture, with those north of the rupture like NSD stretched and those south of it like SPZ condensed by the strong southward directivity (Figures 8c and 8d).

4.2. The 2017 Ezgeleh-Sarpolzahab Aftershocks

Relocated aftershocks are plotted in Figure 4, with full details listed in supporting information Table S1 and traveltimes residuals and relocation vectors shown in supporting information Figures S7–S9. Most of the early aftershocks are located along or just beyond the western and southern edges of the mainshock slip area. The paucity of local station readings makes constraining focal depths challenging, but our preferred solutions generally exceed ~ 10 km, consistent with a concentration within the basement. Where focal mechanisms could be obtained (Table 2 and Figure 4 and 7b) the aftershocks exhibit a variety of slip styles, with only the most recent of those analyzed here—the M_w 5.0 1 April 2018 earthquake, located ~ 10 km west of Sarpolzahab at the southern edge of the mainshock slip area—closely mimicking the mainshock geometry. The M_w 5.5 11 December 2017 Darbandikhan aftershock involves NW-SE left-lateral or NE-SW right-lateral strike slip; the left-lateral nodal plane is conspicuously parallel to the structural fabric of the overlying fold axes. Three aftershocks located southeast and south of the mainshock rupture have strike-slip mechanisms of the opposite sense, consistent with NW-SE right-lateral or NE-SW left-lateral faulting. Three more aftershocks located southwest of the mainshock slip area involve thrusting on approximately N-S oriented, ~ 30 – 60° dip-

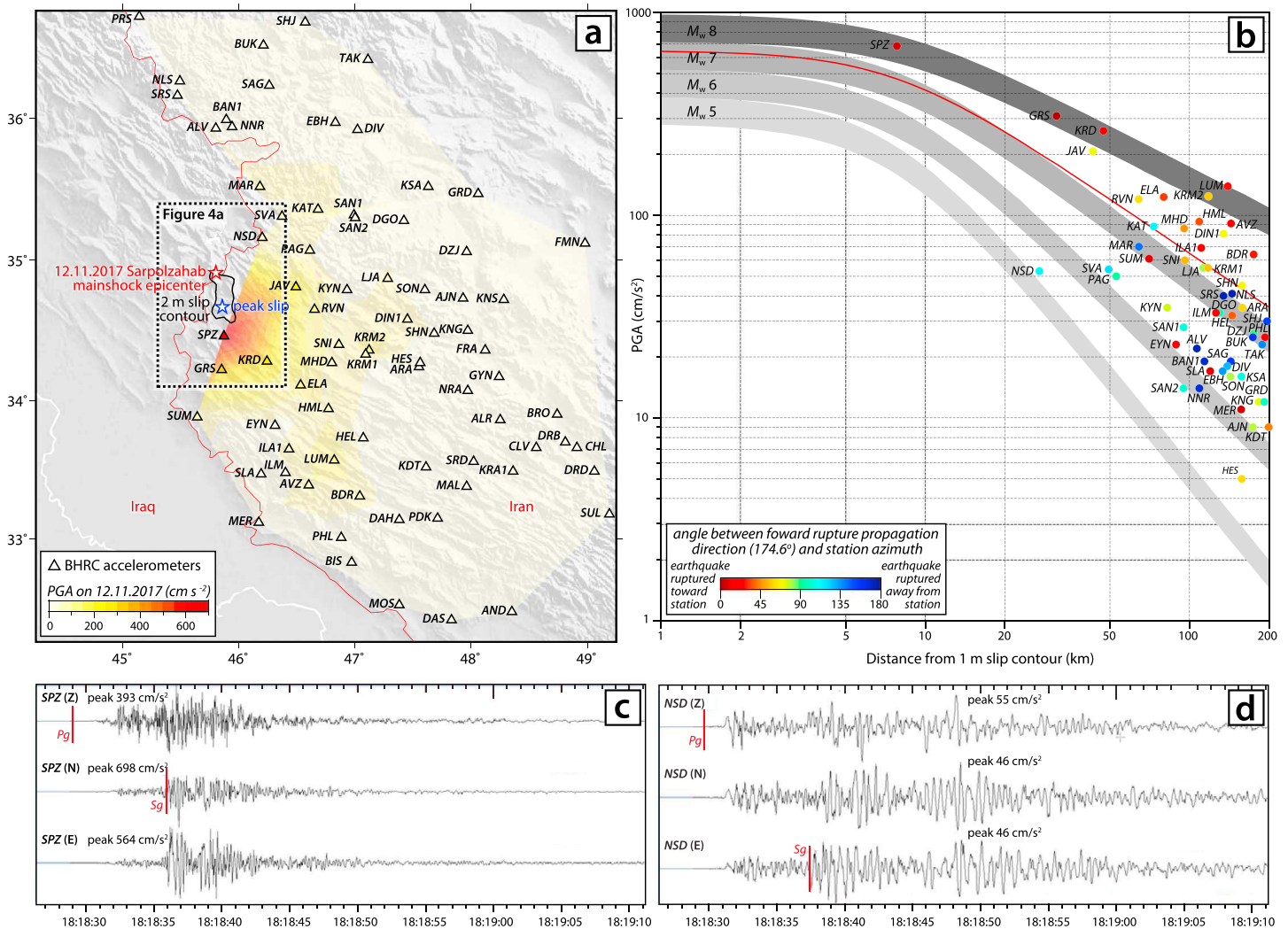


Figure 8. Peak ground accelerations in the 12 November 2017 Ezgeleh-Sarpolzahab mainshock. (a) BHRC stations (triangles) colored by maximum horizontal ground acceleration and interpolated using Delaunay triangulation (Wessel et al., 2013). (b) The same data plotted as a function of earthquake-station distance (x axis, determined relative to the InSAR model 1-m slip contour) and azimuth relative to the rupture forward propagation direction (color, calculated at the InSAR model peak slip location). Curves show the expected decay with distance for shallow thrust earthquakes, calculated using the empirical equations of Ambraseys et al. (2005). For earthquakes of M_w 5, 6, 7, and 8, we show in gray the range of curves for rock, stiff soil, and soft soil sites; for a M_w 7.3 earthquake, we show in red only the stiff soil curve. (c) BHRC accelerometer record at Sarpolzahab (SPZ), ~45 km south of the epicenter, and (d) at Nowsud (NSD), ~45 km NNE of the epicenter. All traces are normalized by PGA, indicated next to the trace. BHRC = Building and Housing Research Network; InSAR = synthetic aperture radar interferometry.

ping nodal planes, that may represent splay faults or ramps at the western edge of the mainshock faulting. However, without better depth control or being able to distinguish the fault and auxiliary nodal planes, it is difficult to further discern the mechanical significance of these aftershocks. Nevertheless, the strong clustering of aftershocks south and west of the mainshock slip area—and therefore in its approximate rupture propagation direction—implies a significant contribution from dynamic triggering. This is because the transient stresses from passing seismic waves were greatest at these azimuths, whereas static stresses are likely more symmetric about the mainshock fault (Freed, 2005; Gomberg et al., 2003).

4.3. The 2018 Mandali Earthquakes

Distinct from the aftershock activity surrounding the Ezgeleh-Sarpolzahab mainshock fault plane is the sequence of events near Mandali in the frontal Lurestan arc starting on 11 January 2018 (Figures 3 and 9). These include an initial M_w ~5.5 earthquake at 06:59 UTC followed quickly and within ~5 km distance by three M_w 5.2–5.3 aftershocks at 07:14, 07:21 and 08:00. All four events have predominantly thrust mechanisms with moderately dipping (~20–70°), approximately NNW or approximately SSE striking nodal planes

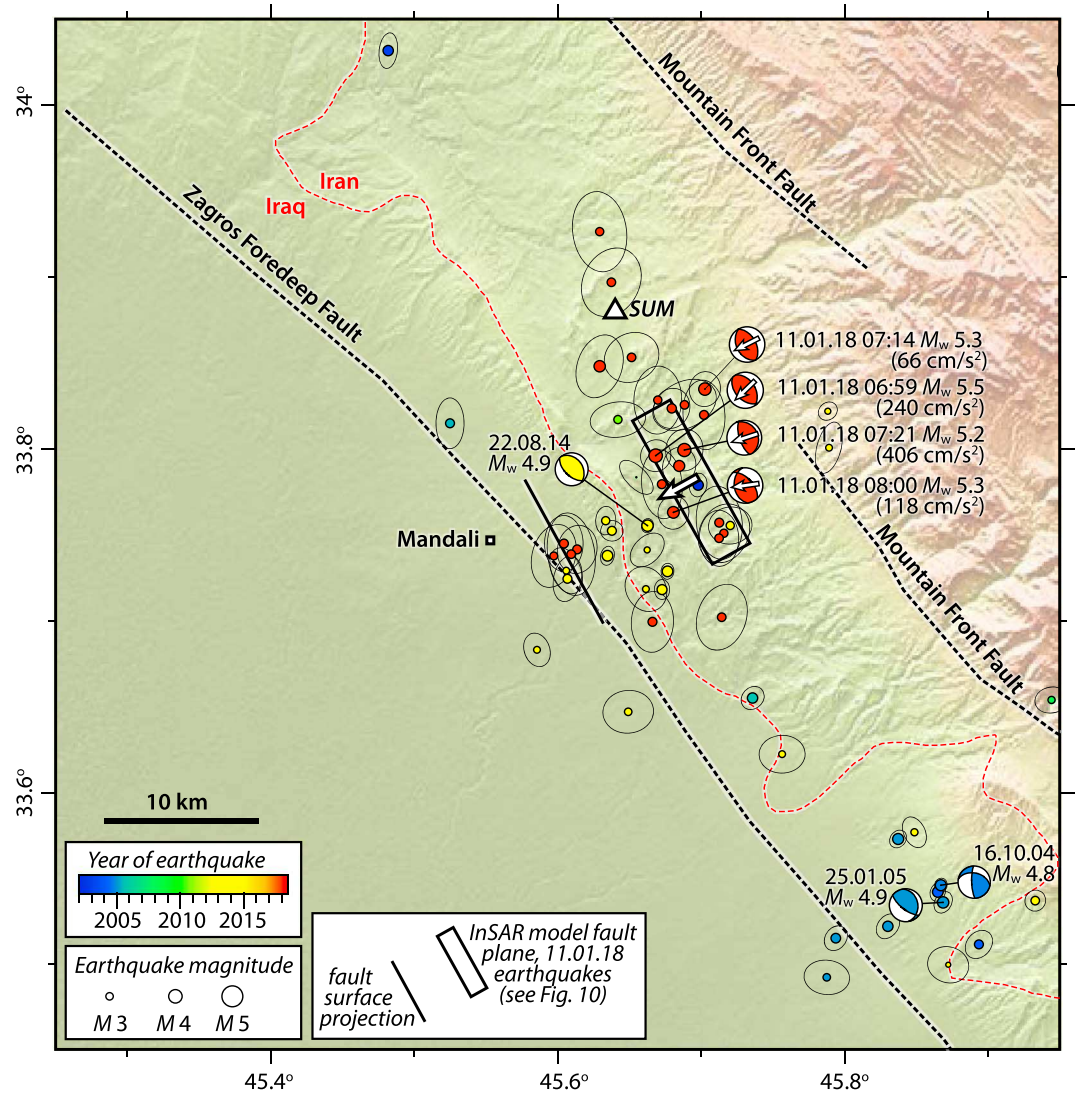


Figure 9. Earthquakes in the Mandali region of the frontal Lurestan arc, plotted at relocated epicentral locations with 90% confidence ellipses. Epicenters and available focal mechanisms are colored by time, with 2018 events in red. The four largest 2018 earthquakes are labeled with date, time, moment magnitude, and the peak ground acceleration as recorded at the Building and Housing Research Network accelerometer station SUM (white triangle). The black rectangle shows the extents of the buried InSAR model fault, with the thick black line its up-dip surface projection. The large white arrow shows the InSAR model fault slip vector; smaller white arrows show slip vectors for the four largest 11 January 2018 earthquakes from seismology (see Table 3) under the assumption that NE dipping nodal planes represent the fault. InSAR = synthetic aperture radar interferometry.

(Table 3). By 14 January 2018, 19 additional events with body wave magnitudes m_b 3.8–4.8 had occurred locally, forming a cloud of aftershocks that extends a few kilometers north, south, and west of the four largest earthquakes.

In the pair of interferograms we processed, the Mandali earthquake cluster is collocated with a approximately NNW-SSE oriented deformation ellipse containing displacements of up to ~ 3 cm toward the satellite (Figures 10a and 10b). These displacements can be reproduced with buried reverse slip on either a NE or SW dipping fault, but we favor the former geometry, which gives rise to slightly smaller residuals and moreover closely matches the location and orientation of the NE dipping Zagros Foredeep Fault (Figures 10c–10f). Our model fault plane parameters are similar to ones obtained by Barnhart et al. (2018) using a slightly different set of InSAR images and their distinct modeling approach; as for the Ezgeleh-Sarpolzahab mainshock, the largest discrepancy is in rake, with our model involving pure reverse slip—consistent with most of the seismic solutions—but Barnhart et al., 2018’s involving a right-lateral component (Table 3). Results

Table 3
Source Parameters of Four Aftershocks Occurring on 11 January 2018 Near Mandali

Date	Time	Source	Strike	Dip	Rake	SV	Longitude	Latitude	Depth	Seismic moment	M_w
11.01.2018	06:59	This paper	328°	44°	99°	226°	45.668° (<i>h</i>)	33.796° (<i>h</i>)	12 km (<i>c</i>)	1.5 × 10 ¹⁷ Nm	5.4
		(acceptable ranges)		39–49°					9–14 km (<i>c</i>)		
		USGS <i>W</i> phase	336°	50°	91°	244°	45.724° (<i>h</i>)	33.713° (<i>h</i>)	13.5 km (<i>c</i>)	2.3 × 10 ¹⁷ Nm	5.5
		USGS body wave	324°	48°	75°	256°	45.724° (<i>h</i>)	33.713° (<i>h</i>)	16 km (<i>c</i>)	1.4 × 10 ¹⁷ Nm	5.4
		GCMT	349°	42°	108°	235°	45.55° (<i>c</i>)	33.80° (<i>c</i>)	12 km (<i>c</i>)	2.9 × 10 ¹⁷ Nm	5.6
11.01.2018	07:14	USGS <i>W</i> phase	330°	50°	88°	243°	45.703° (<i>h</i>)	33.835° (<i>h</i>)	13.5 km (<i>c</i>)	1.0 × 10 ¹⁷ Nm	5.3
11.01.2018	07:21	USGS <i>W</i> phase	332°	22°	81°	252°	45.688° (<i>h</i>)	33.800° (<i>h</i>)	15.5 km (<i>c</i>)	0.9 × 10 ¹⁷ Nm	5.2
11.01.2018	08:00	USGS <i>W</i> phase	317°	57°	69°	262°	45.681° (<i>h</i>)	33.763° (<i>h</i>)	17.5 km (<i>c</i>)	1.2 × 10 ¹⁷ Nm	5.3
<i>Combined</i>		This paper (InSAR)	331°	50°	90°	241°	45.693° (<i>u</i>)	33.781° (<i>u</i>)	11.2 km (<i>u</i>)	7.4 × 10 ¹⁷ Nm	5.8
		(1σ uncertainties)	±4°	±3°	±11°		±0.7 km	±1.0 km	±0.7 km	±0.1 × 10 ¹⁷ Nm	
<i>Combined</i>		Barnhart et al., 2018 (2018; InSAR)	340°	43°	116°	216°	45.70° (<i>p</i>)	33.81° (<i>p</i>)	10.7 km (<i>p</i>)	6.6 × 10 ¹⁷ Nm	5.8

Note. We assume that the NE dipping nodal planes represent the faulting. SV = is the slip vector of the hanging wall relative to the footwall. USGS = U.S. Geological Survey; GCMT = Global Centroid Moment Tensor Catalog. For our body waveform model of the largest Mandali earthquake, sensitivities in dip and centroid depth were determined by fixing these parameters at increments away from the minimum misfit value, solving for the remaining free parameters, and visually assessing the degradation in misfit. Uncertainties shown below our synthetic aperture radar interferometry (InSAR) uniform slip model are from Monte Carlo inversions of 100 synthetic data sets perturbed with realistic noise (supporting information Figure S10). Other pertinent parameters of our uniform slip model include uniform slip of 0.5 m (fixed in the inversion), top depth 9.5 ± 0.5 km, bottom depth 12.8 ± 1.2 km, and length 10.6 ± 2.1 km. *c* = centroid location or depth; *h* = hypocenter location or depth; *u* = uniform slip model fault center point and depth; *p* = distributed slip model peak slip location and depth. Date is formatted as DD.MM.YYYY.

from Monte Carlo inversions of perturbed data sets, from which our estimated uncertainties are drawn, are summarized in supporting information Figure S10.

The InSAR model moment is slightly larger than the summed seismic moments of the four M_w 5.2–5.5 11 January 2018 earthquakes, which led Barnhart et al. (2018) to consider that all four contributed to the observed fringe pattern. However, we find that only the M_w 5.5 06:59 mainshock and the M_w 5.2 07:21 aftershock are exactly collocated with our model fault plane; the 07:14 and 08:00 earthquakes appear slightly down-dip and up-dip of it, respectively. Consequently, it is possible that some postseismic afterslip contributes to the larger InSAR model moment. Peak ground accelerations measured at the nearby BHRC accelerometer station SUM were largest (406 cm/s^2) for the smallest of these events, the 07:21 M_w 5.2 earthquake, and smallest (66 cm/s^2) for the closest of them, the 07:14 M_w 5.3 event, possibly indicative of some strong rupture directivity effects (Figure 9). In particular, we suspect that the 06:59 mainshock ruptured southward across the southern part of the InSAR fault, while the 07:21 event ruptured northward to fill in the northern part.

The center depth of the InSAR model fault plane is well resolved at $\sim 11 \text{ km}$, in close agreement with the centroid depth of $\sim 12 \text{ km}$ for the M_w 5.5 06:59 mainshock from teleseismic body wave modeling (Figure 11a). Fault width and top and bottom fault depths are often poorly resolved for buried reverse earthquakes due to the strong trade-off with slip magnitude, but in testing distributed slip models for the Mandali earthquakes we noticed a propensity toward long, thin slip planes (i.e., high length/width ratios) with depth extents of $\sim 9\text{--}13 \text{ km}$. Cover thickness estimates in this part of the frontal Lurestan arc, between the Zagros Foredeep Fault and the Mountain Front Fault, range from ~ 10 to $\sim 13 \text{ km}$ (Blanc et al., 2003; Emami et al., 2010; Farzipour-Saein et al., 2009; McQuarrie, 2004) and so the Mandali earthquakes may have ruptured the lowermost cover, the uppermost basement, or both. However, the elongate shape of the Mandali slip plane mimics that observed in the 2006 Fin and 2013 Khaki-Shonbe earthquakes, buried reverse faulting events in the Fars arc whose upper and lower limits correspond closely to known weak horizons in the local stratigraphy (Elliott et al., 2015; Roustaei et al., 2010). We speculate that the main Mandali slip plane may be similarly constrained, perhaps by the basal decollement at its lower edge and by the Triassic Dashtak evaporites at its upper one (Casciello et al., 2009).

4.4. Seismicity Prior to 2017, Including the 2013 Qasre Shirin Earthquakes

Our calibrated relocations confirm that a number of earthquakes had occurred in Sarpolzahab and Mandali regions prior to the 2017–2018 earthquakes. The most important of these are the cluster of events near Qasre Shirin in November 2013 (Figure 4). These include two M_w 5.7–5.8 earthquakes on 22 November 2013, a M_w 5.5 event on 24 November 2013, and in total about 40 $M > 3$ earthquakes within a week of the first.

We relocate the Qasre Shirin sequence to the area immediately SW of the 2017 Ezgeleh-Sarpolzahab mainshock rupture area, where it forms an approximately N-S alignment with a distinct southward propagation of activity over the first day of the sequence. Using body waveform modeling, we find that the two largest earthquakes, on 22 November 2013 at 06:51 and 18:30 UTC, have gentle ($\sim 10^\circ$ and $\sim 18^\circ$) NE dipping nodal planes (Figures 11b and 11c and Table 4). Given the predominant reverse sense of motion in both earthquakes, the steeper ($\sim 81^\circ$ and $\sim 72^\circ$) SW dipping nodal planes are probably the auxiliary planes. The third of the main Qasre Shirin earthquakes, on 24 November 2013, has nodal plane dips of $\sim 40^\circ \text{ E}$ or $\sim 58^\circ \text{ W}$ (Figure 11d) and so we cannot be certain of its dip direction. However, we prefer the east dipping fault plane, because the resulting slip vector more closely resembles the $\sim \text{SW}$ slip vector azimuths of the 22 November 2013 earthquakes.

Centroid depths of $\sim 14\text{--}16 \text{ km}$ indicate that the three largest Qasre Shirin earthquakes ruptured mainly or wholly within the basement, but the causative faults are unlikely to be a direct, southward continuation of the one involved in the 2017 Ezgeleh-Sarpolzahab earthquake: the Qasre Shirin epicenters are located $\sim 20 \text{ km}$ too far to the west. Instead, the Qasre Shirin earthquakes likely ruptured east or NE dipping splay faults or ramp and flat structures at the western up-dip edge of the larger basement fault responsible for the Ezgeleh-Sarpolzahab earthquake. Local structural complexities may explain why the Qasre Shirin sequence broke in a quick succession of moderate events rather than as a single throughgoing larger rupture.

We also observe a few earlier earthquakes in close proximity to the 2018 Mandali sequence (Figure 9). In particular, the 2018 earthquakes seem to be reoccupying the location of a condensed cluster of earthquakes in late August 2014. The largest of the earlier events was a M_w 4.9 earthquake on 22 August 2014, with a

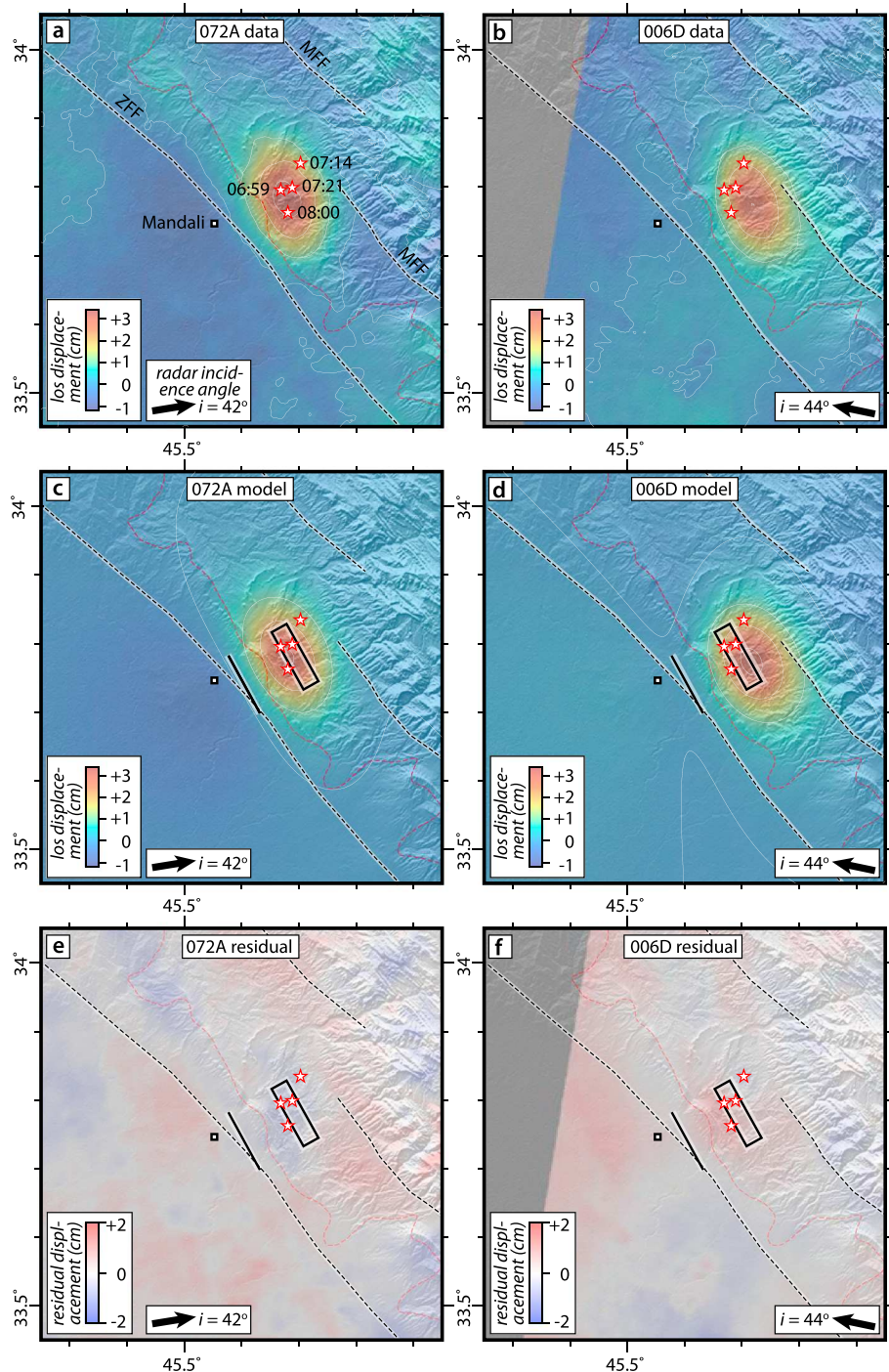


Figure 10. (a) Ascending track 072 (4–16 January 2017) and (b) descending track 006 (31 December 2017 to 12 January 2018) interferograms spanning the 11 January 2018 Mandali earthquakes. The large black arrow shows the radar incidence angle at the synthetic aperture radar interferometry deformation center (with i its inclination from the vertical). White lines show 1-cm line-of-sight displacement contours; positive displacements are toward the satellite and thus in the opposite sense to the satellite look direction. The red stars show calibrated epicenters for the four largest 11 January 2018 events. Dashed lines show the Main Frontal Fault (MFF) and the Zagros Foredeep Fault (ZFF). (c) Ascending and (d) descending model interferograms, with the buried, NE dipping model fault plane and its surface projection indicated by bold black lines. (e) Ascending and (f) descending residual interferograms (model minus data).

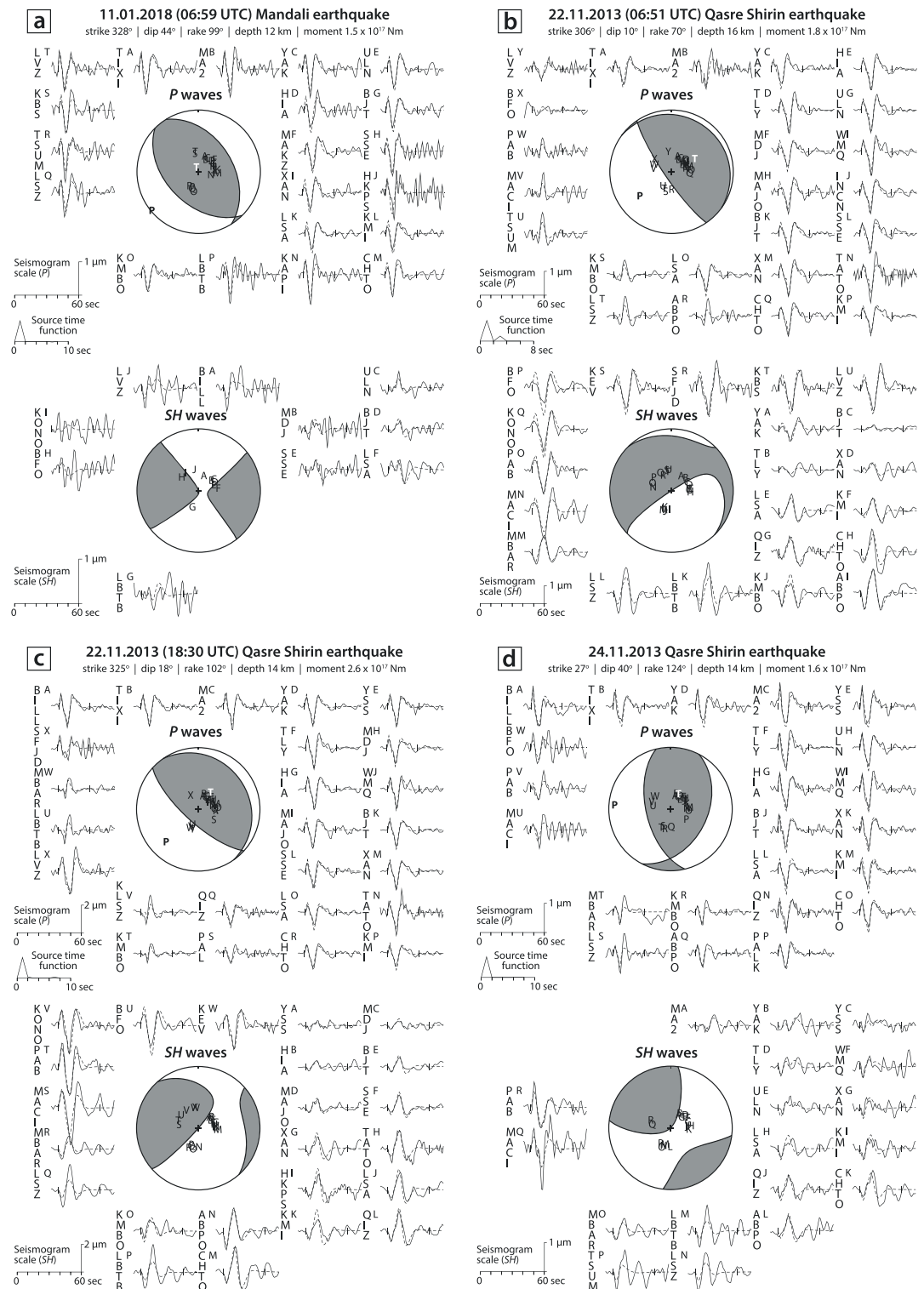


Figure 11. Telesismic body waveform models of (a) the 11 January 2018 (06:59 UTC) Mandali earthquake, (b) the 22 November 2013 (06:51 UTC) Qasre Shirin earthquake, (c) the 22 November 2013 (18:30 UTC) Qasre Shirin earthquake, and (d) the 24 November 2013 Qasre Shirin earthquake. The plot layout is the same as for Figure 7a.

Table 4
Source Parameters of the 22–24 November 2013 Qasre Shirin Earthquakes

Date	Time	Source	Strike	Dip	Rake	Strike	Dip	Rake	Longitude	Latitude	Depth	Seismic moment	M_w
22.11.2013	06:51	This paper	306°	10°	70°	146°	81°	93°	45.450° (<i>h</i>)	34.491° (<i>h</i>)	16 km (<i>c</i>)	1.8 × 10 ¹⁷ Nm	5.4
		(acceptable range)		7–24°							13–18 km		
		USGS CMT	335°	19°	102°	142°	72°	86°	45.482° (<i>h</i>)	34.457° (<i>h</i>)	12.7 km (<i>c</i>)	4.1 × 10 ¹⁷ Nm	5.7
		USGS body wave	334°	10°	94°	149°	80°	89°	45.482° (<i>h</i>)	34.457° (<i>h</i>)	6 km (<i>c</i>)	3.6 × 10 ¹⁷ Nm	5.6
		GCMT	339°	24°	109°	139°	68°	82°	45.31° (<i>c</i>)	34.28° (<i>h</i>)	18.1 km (<i>c</i>)	4.0 × 10 ¹⁷ Nm	5.7
22.11.2013	18:30	This paper	325°	18°	102°	132°	72°	86°	45.518° (<i>h</i>)	34.370° (<i>h</i>)	14 km (<i>c</i>)	2.6 × 10 ¹⁷ Nm	5.5
		(acceptable range)		14–35°							12–16 km		
		USGS <i>W</i> phase	351°	27°	113°	145°	65°	79°	45.611° (<i>h</i>)	34.308° (<i>h</i>)	13.5 km (<i>c</i>)	5.8 × 10 ¹⁷ Nm	5.8
		USGS CMT	351°	22°	128°	131°	73°	76°	45.611° (<i>h</i>)	34.308° (<i>h</i>)	10 km (<i>c</i>)	5.6 × 10 ¹⁷ Nm	5.8
		USGS CMT	354°	25°	127°	135°	70°	74°	45.611° (<i>h</i>)	34.308° (<i>h</i>)	12 km (<i>c</i>)	5.4 × 10 ¹⁷ Nm	5.8
		USGS body wave	325°	21°	89°	146°	69°	91°	45.611° (<i>h</i>)	34.308° (<i>h</i>)	10 km (<i>c</i>)	2.9 × 10 ¹⁷ Nm	5.6
24.11.2013	18:05	GCMT	354°	35°	125°	134°	62°	68°	45.44° (<i>c</i>)	34.22° (<i>h</i>)	13.9 km (<i>c</i>)	4.4 × 10 ¹⁷ Nm	5.7
		This paper	27°	40°	124°	167°	58°	65°	45.481° (<i>h</i>)	34.269° (<i>h</i>)	14 km (<i>c</i>)	1.6 × 10 ¹⁷ Nm	5.4
		(acceptable range)		32–48°							12–16 km		
		USGS CMT	25°	35°	141°	148°	69°	61°	45.617° (<i>h</i>)	34.177° (<i>h</i>)	15.4 km (<i>c</i>)	3.0 × 10 ¹⁷ Nm	5.6
		USGS body wave	10°	41°	119°	154°	55°	67°	45.617° (<i>h</i>)	34.177° (<i>h</i>)	14 km (<i>c</i>)	1.5 × 10 ¹⁷ Nm	5.4
GCMT	13°	41°	116°	160°	54°	69°	45.43° (<i>c</i>)	34.18° (<i>h</i>)	18.7 km (<i>c</i>)	2.3 × 10 ¹⁷ Nm	5.5		

Note. USGS = U.S. Geological Survey; GCMT = Global Centroid Moment Tensor Catalog. For the second earthquake, the USGS lists two “Centroid Moment Tensor” solutions. For all three earthquakes, we consider that the first listed nodal plane—dipping toward the approximately NE or approximately east—likely represents the fault plane (see text). If this is correct, our body wave solutions would imply slip vector azimuths of 236°, 222°, and 256° in the three earthquakes. Sensitivities in the dip of the NE or east dipping nodal planes and in centroid depth were determined by fixing these parameters at increments away from the minimum misfit value, solving for the remaining free parameters, and visually assessing the worsening misfit. *c* = centroid location or depth; *h* = hypocenter location or depth; *u* = uniform slip model fault center point and depth.

GCMT mechanism similar to those of the larger 2018 Mandali earthquakes. Located immediately west of the 11 January 2018 fault plane, the 22 August 2014 earthquake may have ruptured the neighboring (up-dip) portion of the Zagros Foredeep Fault.

Prior to 2013, the largest instrumentally recorded earthquake in the western Lurestan arc was a M_w 5.6 earthquake on 11 January 1967 located between Mandali and Sarpolzahab. McKenzie (1972) assigned this event a predominantly reverse mechanism using teleseismic first motion polarities, and Ni and Barazangi (1986) later determined a centroid depth of 10 ± 4 km using body waveform modeling. We relocated its epicenter to 34.083°N , 45.558°E , ~ 38 km north of Mandali and ~ 11 km northeast of the Iranian town of Naft Shahr, after which the earthquake is labeled in Figure 3. This places the epicenter between the surface projections of the NE dipping Zagros Foredeep and Mountain Front Faults, making the former the most likely causative fault. The probable fault plane of McKenzie's (1972) solution dips 40° NE and has slip vector azimuth 230° , close to the values we obtained for the largest Mandali earthquakes.

5. Discussion

The M_w 7.3 Ezgeleh-Sarpolzahab earthquake ruptured a gently eastward dipping oblique (dextral-thrust) fault beneath the northwestern Lurestan arc. The up-dip edge of the 2017 rupture plane corresponds closely with the northwestern margin of the Lurestan arc (Figure 4) and repeated earthquakes on this fault would in the long-term give rise to the ~ 1 km topographic contrast between the arc and the neighboring Kirkuk embayment. Reverse faults responsible for large frontal escarpments in the Zagros SFB are collectively named the Mountain Front Fault, after Berberian (1995; Figure 12a). However, the faulting involved in the Ezgeleh-Sarpolzahab earthquake is distinct in key regards from sections of the Mountain Front Fault elsewhere in the Zagros; in this discussion we assign it a new name, the "Ezgeleh-Sarpolzahab fault," for clarity (Figure 12b). The first key difference is that earthquakes along the Mountain Front Fault mostly have ~ 20 – 60° dipping fault planes (Figures 2a and 12a), significantly steeper than the $\sim 15^\circ$ Ezgeleh-Sarpolzahab fault. Second, most earthquakes on the Mountain Front Fault have predominantly reverse mechanisms, whereas the Ezgeleh-Sarpolzahab earthquake involved SW directed slip highly oblique to the local approximately N-S range front topography. Finally, the Mountain Front Fault emerges upward from the basement into the lower to middle sedimentary cover—confirmed by shallow centroid depths (Nissen et al., 2011)—where it controls the growth of large surface anticlines (e.g., Berberian, 1995; Blanc et al., 2003). This explains why the Mountain Front Fault had previously been mapped in the Sarpolzahab region as an echelon set of short, NW striking segments, which parallel the regional trend in fold axes (as shown in Figures 2, 3 and 12a). In reality, the N-S Ezgeleh-Sarpolzahab fault is at a high angle to overlying folds, from which it must be detached (Figure 12b). This inference is supported by observations of afterslip following the Ezgeleh-Sarpolzahab earthquake, which is focused at the up-dip limit of coseismic slip on a subhorizontal structure centered at ~ 10 to 14 km depth (Barnhart et al., 2018).

Though a few of the Ezgeleh-Sarpolzahab aftershocks exhibit strike-slip mechanisms, there is no clear indication in the seismicity pattern of a major N-S subvertical strike-slip fault separating these regions: the "Khanaqin fault" of Hessami et al. (2001) and Bahroudi and Talbot (2003; Figure 12). That NW-SE trending anticlines appear truncated at the boundary between the Lurestan arc and Kirkuk embayment is likely related to differences in stratigraphic level and/or basement depth that inhibit folds from propagating laterally between the two regions, as is implicated across the Balarud Line (Allen & Talebian, 2011). The SW directed slip vector of the 2017 mainshock is almost exactly perpendicular to the strike of the Main Recent Fault (Figure 4) and so despite the high obliquity, the Ezgeleh-Sarpolzahab fault cannot account for any NW-SE oriented dextral shear in the NW Zagros (Talebian & Jackson, 2004; Vernant et al., 2004).

The Ezgeleh-Sarpolzahab mainshock ruptured southward at ~ 1.5 – 2.0 km/s, at the lower end of the range of rupture velocities observed in large earthquakes globally (e.g., Chouneet et al., 2018). The strong directivity is clearly responsible for the focusing of damage at the south end of the rupture plane, in the city of Sarpolzahab and the Zahab plain north of it (Figures 4 and 7a). Nevertheless, the human impact of this earthquake was far lower than for similar-sized earthquakes at Dasht-e Bayaz in 1968, Tabas in 1978, Rudbar in 1990, and the smaller (M_w 6.6) Bam earthquake in 2003, which each killed $>10,000$ people. Maximum horizontal ground accelerations in the Ezgeleh-Sarpolzahab earthquake were, on average, about as expected for a shallow dip-slip event of its magnitude (Ambraseys et al., 2005), and in fact, ground accelerations in Sarpolzahab itself were large considering its distance from the rupture (Fig 7b). Sarpolzahab was badly damaged in the

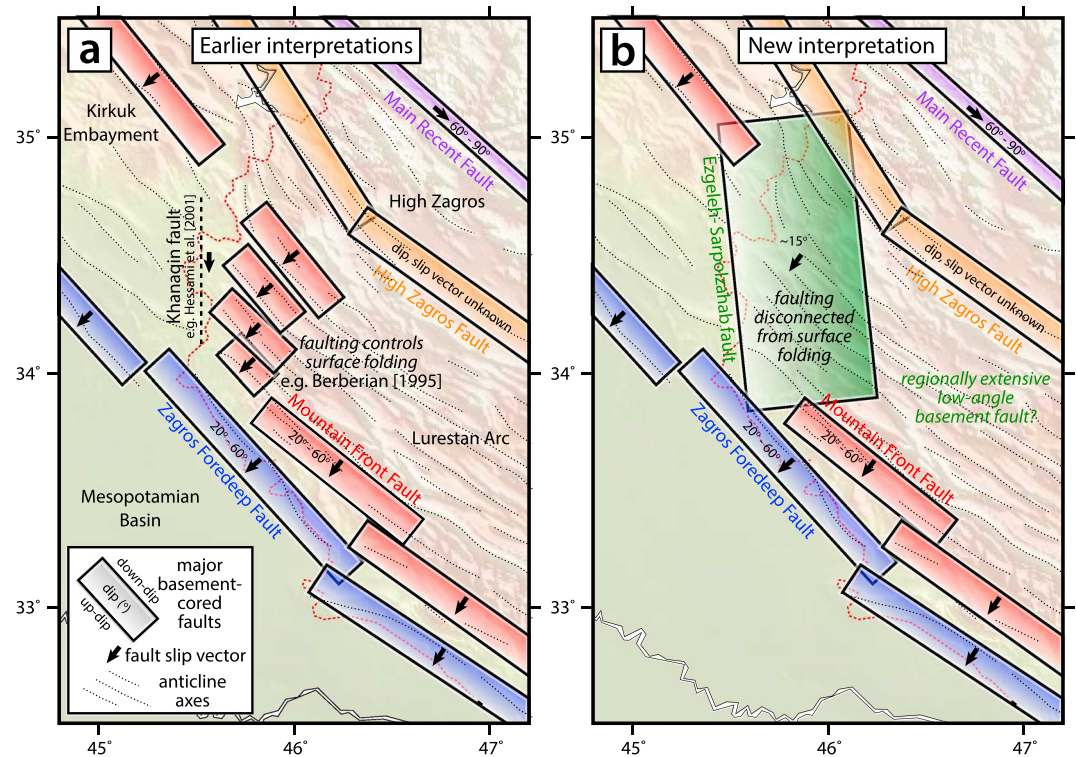


Figure 12. Schematic illustrations of the geometry of basement-cored faults in the western Lurestan arc, showing (a) earlier and (b) new interpretations. Faults are colored with darker shading down-dip and labeled with their approximate dip values—estimated wherever possible from earthquake focal mechanisms—and slip vectors (showing motion of the hanging wall relative to the footwall). (a) Earlier interpretations of Berberian (1995), in which the Zagros Foredeep Fault and Mountain Front Fault control frontal fold growth throughout the Lurestan arc, and Hessami et al. (2001) and Sepehr and Cosgrove (2004), in which a dextral “Khanaqin fault” separates the Lurestan arc from the Kirkuk embayment. (b) Our new interpretation, in which the boundary between the Lurestan arc and Kirkuk embayment is controlled by the oblique thrust/right lateral, $\sim 15^\circ$ approximately east dipping Ezgeleh-Sarpolzahab fault. This fault trends at a high angle to overlying fold axes, suggesting that faulting and folding are decoupled.

late 1980s during fighting in the Iran-Iraq war and was rebuilt to improved standards afterward, and we suspect that this is the primary reason for the smaller number of fatalities (~ 600) in the 2017 earthquake.

The southward mainshock propagation direction is also responsible for the concentration of aftershocks around the southern end of the rupture plane, consistent with patterns observed in several other strongly unilateral earthquakes (Gomberg et al., 2003; Freed, 2005). An outstanding question is whether the January 2018 Mandali sequence, ~ 80 km (about two fault lengths) south of the southern edge of the Ezgeleh-Sarpolzahab rupture plane, was itself triggered by the mainshock. Barnhart et al. (2018) show that Coulomb stresses on the Zagros Foredeep Fault at Mandali were raised by slip in the Ezgeleh-Sarpolzahab mainshock by ~ 0.001 – 0.002 MPa, roughly one tenth of the values normally invoked in cases of static triggering (e.g., Freed, 2005). However, dynamic stresses may have exceeded these values and would have been enhanced in the Mandali region by the southward mainshock rupture directivity. The Zagros Foredeep Fault may also have been stressed locally by an earlier M_w 4.9 earthquake in August 2014, which seems to have occurred directly up-dip from the largest January 2018 earthquakes (Figure 9). The Mandali earthquakes are rather typical of those in the frontal Lurestan arc, exhibiting tight clustering in space, time, and magnitude (Copley et al., 2015; Motagh et al., 2015; Nippress et al., 2017). We suspect that structural complexities associated with these frontal faults and folds, as well as weak stratigraphic horizons in the middle and lower sedimentary cover, may act to limit earthquake rupture areas and moment magnitudes in this region in a similar manner to the Fars arc (Elliott et al., 2015; Nissen et al., 2011).

An important consideration for regional seismic hazard assessment is whether or not gently dipping, seismogenic basement faulting implicated in the 2017 Ezgeleh-Sarpolzahab earthquake underlies other parts of the Lurestan arc. On the one hand, relocated seismicity concentrates around the edge of the arc and the few

Acknowledgments

E. N. acknowledges support from the National Science Foundation through award EAR 1524815, the Natural Sciences and Engineering Research Council of Canada through Discovery Grant 2017-04029, the Canada Foundation for Innovation, the British Columbia Knowledge Development Fund, and the Canada Research Chair program. W. D. B. is supported by National Aeronautics and Space Administration New Investigators Program award NNX16AH53G and the high performance computational resources of the University of Iowa. J. R. E. acknowledges support from the Royal Society through a University Research Fellowship. InSAR interferograms were made using freely available Copernicus Sentinel data (2017; <https://scihub.copernicus.eu/>). All broadband seismograms were downloaded from the Incorporated Research Institutions for Seismology (IRIS) Data Management Center (<https://ds.iris.edu/ds/nodes/dmc/>). Accelerograms, and peak ground acceleration measurements were downloaded from the Building and Housing Research Network of Iran (<https://ismn.bhrc.ac.ir/en/>). Phase arrival time data were downloaded from the Bulletin of the International Seismological Centre Bulletin (<http://www.isc.ac.uk/iscbulletin/>). These data include picks gathered from the U.S. Geological Survey, the Iranian National Seismograph Network, the Building and Housing Research Network, the Iranian Seismological Center, the China-Iran Geological Geophysical Survey in the Iranian Plateau (CIGSIP), the Iraqi Broadband Seismic Network, the Iraqi Seismic Observatory (ISO), the Kurdistan Seismic Network, and the Jordan Seismic Network. Codes used to model these data sets were obtained from the authors of references listed in section 3. CIGSIP is a joint project of the Department of Earth Sciences at the Institute for Advanced Studies in Basic Sciences, University of Zanjan, the Institute of Geology and Geophysics at the Chinese Academy of Sciences, and the Research Institute of Earth Sciences at the Geological Survey of Iran, and field work related to the operation of the CIGSIP seismic network in NW Iran was financially supported by the Strategic Priority Research Program (B) of the Chinese Academy of Sciences (Grant XDB03010802). The ISO is operated by the Seismological Laboratory of the University of Basra (SLUB) with funding from IRIS, the University of Arkansas at Little Rock, and Lawrence Livermore National Laboratory. All of the maps in this paper were plotted using *Generic Mapping Tools* (Wessel et al., 2013), which is supported by the National

$M_w > 5$ earthquakes occurring within its interior have moderately dipping nodal planes and relatively shallow centroid depths (Figure 3). Throughout the Zagros SFB, earthquakes with confirmed low-angle fault planes and at unequivocal basement depths (i.e., blue mechanisms in Figure 2) are mostly restricted to the major inflections in the trend of the mountain belt, along the northwestern and southeastern margins of the Lurestan arc and in the Oman syntaxis. This hints that these faults may help control the gross lobate morphology of the SFB. On the other hand, a distinct seismic interface imaged in a receiver function profiles across the southern Lurestan arc, subhorizontal in SW-NE profile view and at the same ~ 17 km depth as the Ezgeleh-Sarpolzahab fault, hints that such faulting may be regionally extensive (Motaghi, Shabaniyan, & Kalvandi, 2017).

Regrettably, the GPS coverage required to infer whether strain is accumulating on such a structure is absent from this part of the Zagros (Walpersdorf et al., 2006). However, we consider it unlikely that this interface is everywhere seismogenic, since this would imply an average moment release rate of $\sim 5 \times 10^{18}$ Nm/year across the $\sim 40,000$ km² surface area of the arc (using range-perpendicular shortening of ~ 4 mm/year (Vernant et al., 2004; Walpersdorf et al., 2006)). This is equivalent to a $M_w \sim 7$ rupture on average every year, or a $M_w \sim 8$ every ~ 250 years, but there is no indication of such earthquakes in either the instrumental or historical catalogues (Ambraseys & Melville, 1982; Engdahl et al., 2006; Shahvar et al., 2013). Even larger earthquakes, of the type observed in the Himalayan arc where the largest may exceed M_w 8.6 (e.g., Bilham et al., 2001), could have average repeat intervals that exceed the historical record, which is considered reliable only as far back as the 7th century CE (Ambraseys & Melville, 1982). Though we consider such a “great earthquake” on the Lurestan arc unlikely, we caution that the available data cannot definitively rule one out. The potential throughout the Lurestan arc for rare earthquakes of similar or larger magnitude to the 2017 Ezgeleh-Sarpolzahab earthquake therefore needs to be investigated further, especially using dense GPS data that could help reveal whether or not the extensive regional seismic interface is locked and accumulating strain.

6. Conclusions

The 12 November 2017 M_w 7.3 Ezgeleh-Sarpolzahab earthquake involved oblique (dextral-thrust) slip across a broad ($\sim 40 \times 20$ km), gently dipping ($\sim 15^\circ$) rupture plane in the basement of the northwestern Lurestan arc. This geometry accounts for the unexpectedly large magnitude, since previous well-studied earthquakes in the Zagros SFB involved steeper reverse faults at shallower depths that were limited in rupture area by weak sedimentary layers. The earthquake nucleated near Ezgeleh and ruptured southward to near Sarpolzahab, where the worst damage occurred. Early aftershocks cluster at the southern and western edges of the mainshock slip area and may also include a cluster of events at Mandali (Iraq), a further ~ 80 km to the south near Mandali (Iraq). The spatial bias in aftershock activity mimics the southward unilateral rupture propagation direction, implying a significant component of dynamic triggering. The east dipping fault responsible for the Ezgeleh-Sarpolzahab earthquake likely accounts for the ~ 1 km step in elevation between the high Lurestan arc and the low Kirkuk embayment but seems to be distinct from segments of the Mountain Front Fault that generate steep range front topography elsewhere in the Zagros. The Ezgeleh-Sarpolzahab fault may be part of an extensive structure imaged in receiver functions underlying much of the Lurestan arc, but if so it is unlikely to be seismogenic everywhere since this would imply moment release rates that far exceed those observed either instrumentally or historically. Nevertheless, this earthquake highlights the need for denser GPS coverage in the NW Zagros that could help distinguish strain accumulation on a regional low-angle structure.

References

- Abdollahie-Fard, I., Braathen, A., Mokhtari, M., & Alavi, S. A. (2006). Interaction of the Zagros Fold–Thrust Belt and the Arabian-type, deep-seated folds in the Abadan Plain and the Dezful Embayment, SW Iran. *Petroleum Geoscience*, *12*(4), 347–362.
- Abdulnaby, W., Mahdi, H., Numan, N. M. S., & Al-Shukri, H. (2014). Seismotectonics of the Bitlis-Zagros Fold and Thrust Belt in Northern Iraq and Surrounding Regions from Moment Tensor Analysis. *Pure and Applied Geophysics*, *171*, 1237–1250.
- Agard, P., Omrani, J., Jolivet, L., & Mouthereau, F. (2005). Convergence history across Zagros (Iran): Constraints from collisional and earlier deformation. *International Journal of Earth Sciences*, *94*, 401–419.
- Ahmadhadi, F., Lacombe, O., & Daniel, J.-M. (2007). Early reactivation of basement faults in Central Zagros (SW Iran): Evidence from pre-folding fracture populations in Asmari Formation and Lower Tertiary Paleogeography. In *Thrust Belts and Foreland Basins* (pp. 205–228). Berlin Heidelberg: Springer.

Science Foundation. Finally, we are grateful to Ryan Gold, the Associate Editor, and three anonymous reviewers for their comments on the manuscript.

- Alavi, M. (2004). Regional stratigraphy of the Zagros fold-thrust belt of Iran and its proforeland evolution. *American Journal of Science*, *304*, 1–20.
- Allen, M. B., Saville, C., Blanc, E. J.-P., Talebian, M., & Nissen, E. (2013). Orogenic plateau growth: Expansion of the Turkish-Iranian Plateau across the Zagros fold-and-thrust belt. *Tectonics*, *32*, 1–20. <https://doi.org/10.1002/tect.20025>
- Allen, M. B., & Talebian, M. (2011). Structural variation along the Zagros and the nature of the Dezful Embayment. *Geological Magazine*, *148*, 911–924.
- Allmann, B. P., & Shearer, P. M. (2009). Global variations of stress drop for moderate to large earthquakes. *Journal of Geophysical Research*, *114*, B01310. <https://doi.org/10.1029/2008JB005821>
- Ambraseys, N. N., Douglas, J., Sarma, S. K., & Smit, P. M. (2005). Equations for the estimation of strong ground motions from shallow crustal earthquakes using data from Europe and the Middle East: Horizontal peak ground acceleration and spectral acceleration. *Bulletin of Earthquake Engineering*, *3*(1), 1–53.
- Ambraseys, N. N., & Melville, C. P. (1982). *A history of Persian earthquakes*. Cambridge: Cambridge University Press.
- Bahroudi, A., & Talbot, C. J. (2003). The configuration of the basement beneath the Zagros Basin. *Journal of Petroleum Geology*, *26*, 257–282.
- Barnhart, W. D., Brengman, C. M. J., Li, S., & Peterson, K. E. (2018). Ramp-flat basement structures of the Zagros Mountains inferred from co-seismic slip and afterslip of the 2017 M_w 7.3 Darbandikhan, Iran/Iraq earthquake. *Earth and Planetary Science Letters*, *496*, 96–107.
- Barnhart, W. D., & Lohman, R. B. (2010). Automated fault model discretization for inversions for coseismic slip distributions. *Journal of Geophysical Research*, *115*, B10419. <https://doi.org/10.1029/2010JB007545>
- Barnhart, W. D., & Lohman, R. B. (2013). Phantom earthquakes and triggered aseismic creep: Vertical partitioning of strain during earthquake sequences in Iran. *Geophysical Research Letters*, *40*, 819–823. <https://doi.org/10.1002/grl.50201>
- Barnhart, W. D., Lohman, R. B., & Mellors, R. J. (2013). Active accommodation of plate convergence in Southern Iran: Earthquake locations, triggered aseismic slip, and regional strain rates. *Journal of Geophysical Research: Solid Earth*, *118*, 5699–5711. <https://doi.org/10.1002/jgrb.50380>
- Berberian, M. (1995). Master blind thrust faults hidden under the Zagros folds: Active basement tectonics and surface morphotectonics. *Tectonophysics*, *241*, 193–224.
- Berberian, M., & Yeats, R. S. (1999). Patterns of historical earthquake rupture in the Iranian Plateau. *Bulletin of the Seismological Society of America*, *89*(1), 120–139.
- Bergman, E. A., & Solomon, S. C. (1990). Earthquake swarms on the Mid-Atlantic Ridge—Products of magmatism or extensional tectonics? *Journal of Geophysical Research*, *95*, 4943–4965.
- Bilham, R., Gaur, V. K., & Molnar, P. (2001). Himalayan seismic hazard. *Science*, *293*(5534), 1442–1444.
- Blanc, E. J.-P., Allen, M. B., Inger, S., & Hassani, H. (2003). Structural styles in the Zagros Simple Folded Zone, Iran. *Quarterly Journal of the Geological Society of London*, *160*, 401–412.
- Bretis, B., Bartl, N., & Grasmann, B. (2011). Lateral fold growth and linkage in the Zagros fold and thrust belt (Kurdistan, NE Iraq). *Basin Research*, *23*, 615–630.
- Carruba, S., Perotti, C. R., Buonaguro, R., Calabrò, R., Carpi, R., & Naini, M. (2006). Structural pattern of the Zagros fold-and-thrust belt in the Dezful Embayment (SW Iran). *Geological Society of America Special Paper*, *414*, 11–32.
- Casciello, E., Vergés, J., Saura, E., Casini, G., Fernández, N., Blanc, E., et al. (2009). Fold patterns and multilayer rheology of the Lurestan Province, Zagros Simply Folded Belt (Iran). *Journal of the Geological Society of London*, *166*, 947–959.
- Chen, L., Jiang, M., Talebian, M., Ghods, A., Chung, S.-L., Ai, Y., et al. (2016). New Seismic Array Observation in the Northwestern Iranian Plateau. In *EGU General Assembly Conference Abstracts*, *18* (3427 pp.). Vienna Austria.
- Chen, K., Xu, W., Mai, P. M., Gao, H., Zhang, L., & Ding, X. (2018). The 2017 M_w 7.3 Sarpol Zahāb Earthquake, Iran: A compact blind shallow-dipping thrust event in the mountain front fault basement. *Tectonophysics*, *747–748*, 108–114.
- Choumet, A., Vallée, M., Causse, M., & Courboulex, F. (2018). Global catalog of earthquake rupture velocities shows anticorrelation between stress drop and rupture velocity. *Tectonophysics*, *733*, 148–158.
- Clarke, P. J., Paradissis, D., Briole, P., England, P. C., Parsons, B. E., Billiris, H., et al. (1997). Geodetic investigation of the 13 May 1995 Kozani-Grevena (Greece) earthquake. *Geophysical Research Letters*, *24*, 707–710.
- Copley, A., Karasozen, E., Oveisi, B., Elliott, J. R., Samsonov, S., & Nissen, E. (2015). Seismogenic faulting of the sedimentary sequence and laterally variable material properties in the Zagros Mountains (Iran) revealed by the August 2014 Murmuri (E. Dehloran) earthquake sequence. *Geophysical Journal International*, *203*, 1436–1459.
- de Vera, J., Gines, J., Oehlers, M., McClay, K., & Doski, J. (2009). Structure of the Zagros fold and thrust belt in the Kurdistan Region, northern Iraq. *Trabajos de Geología*, *29*, 213–217.
- Derikvand, B., Alavi, S. A., Abdollahie Fard, I., & Hajjalibeigi, H. (2018). Folding style of the Dezful Embayment of Zagros Belt: Signatures of detachment horizons, deep-rooted faulting and syn-deformation deposition. *Marine and Petroleum Geology*, *91*, 501–518.
- Ding, K., He, P., Wen, Y., Chen, Y., Wang, D., Li, S., & Wang, Q. (2018). The 2017 M_w 7.3 Ezgeleh, Iran earthquake determined from InSAR measurements and teleseismic waveforms. *Geophysical Journal International*, *215*, 1728–1738.
- Edgell, H. (1991). Proterozoic salt basins of the Persian Gulf area and their role in hydrocarbon generation. *Precambrian Research*, *54*, 1–14.
- Elliott, J. R., Bergman, E. A., Copley, A. C., Ghods, A. R., Nissen, E. K., Oveisi, B., et al. (2015). The 2013 M_w 6.2 Khaki-Shonbe (Iran) earthquake: Insights into seismic and aseismic shortening of the Zagros sedimentary cover. *Earth and Space Science*, *2*, 435–471.
- Elliott, J. R., Biggs, J., Parsons, B., & Wright, T. J. (2008). InSAR slip rate determination on the Altyn Tagh Fault, northern Tibet, in the presence of topographically correlated atmospheric delays. *Geophysical Research Letters*, *35*, L12309. <https://doi.org/10.1029/2008GL033659>
- Elliott, J. R., Nissen, E. K., England, P. C., Jackson, J. A., Lamb, S., Li, Z., et al. (2012). Slip in the 2010–2011 Canterbury earthquakes, New Zealand. *Journal of Geophysical Research*, *117*, B03401. <https://doi.org/10.1029/2011JB008868>
- Emami, H., Vergés, J., Nalpas, T., Gillespie, P., Sharp, I., Karpuz, R., et al. (2010). Structure of the Mountain Front Flexure along the Anaran anticline in the Pusht-e-Kuh Arc (NW Zagros, Iran): Insights from sand box models. *Geological Society, London, Special Publications*, *330*, 155–178.
- Engdahl, R. E., Jackson, J. A., Myers, S. C., Bergman, E. A., & Priestley, K. (2006). Relocation and assessment of seismicity in the Iran region. *Geophysical Journal International*, *167*, 761–778.
- Farzipour-Saein, A., Yassaghi, A., Sherkati, S., & Koyi, H. (2009). Mechanical stratigraphy and folding style of the Lurestan region in the Zagros Fold-Thrust Belt, Iran. *Journal of the Geological Society of London*, *166*(6), 1101–1115.
- Feng, W., Samsonov, S., Almeida, R., Yassaghi, A., Li, J., Qiu, Q., et al. (2018). Geodetic constraints of the 2017 M_w 7.3 Sarpol Zahab, Iran earthquake, and its implications on the structure and mechanics of the northwest Zagros thrust-fold belt. *Geophysical Research Letters*, *45*, 6853–6861. <https://doi.org/10.1029/2018GL078577>

- Freed, A. M. (2005). Earthquake triggering by static, dynamic, and postseismic stress transfer. *Annual Review of Earth and Planetary Sciences*, 33, 335–367.
- Funning, G. J., Parsons, B., Wright, T. J., Jackson, J. A., & Fielding, E. J. (2005). Surface displacements and source parameters of the 2003 Bam (Iran) earthquake from Envisat advanced synthetic aperture radar imagery. *Journal of Geophysical Research*, 110, B09406. <https://doi.org/10.1029/2004JB003338>
- Futterman, W. I. (1962). Dispersive body waves. *Journal of Geophysical Research*, 67, 5279–5291.
- Ghods, A., Rezapour, M., Bergman, E., Mortezaejad, G., & Talebian, M. (2012). Relocation of the 2006 Mw 6.1 Silakhour, Iran, earthquake sequence: Details of fault segmentation on the main recent fault. *Bulletin of the Seismological Society of America*, 102, 398–416.
- Ghods, A., Shabaniyan, E., Bergman, E., Faridi, M., Donner, S., Mortezaejad, G., & Aziz-Zanjani, A. (2015). The Varzaghan-Ahar, Iran, earthquake doublet (M_w 6.4, 6.2): Implications for the geodynamics of northwest Iran. *Geophysical Journal International*, 203, 522–540.
- Gomberg, J., Bodin, P., & Reasenberg, P. A. (2003). Observing earthquakes triggered in the near field by dynamic deformations. *Bulletin of the Seismological Society of America*, 93, 118–138.
- Hayes, G. P. (2017). The finite, kinematic rupture properties of great-sized earthquakes since 1990. *Earth and Planetary Science Letters*, 468, 94–100.
- Hessami, K., Koyi, H. A., & Talbot, C. J. (2001). The significance of strike-slip faulting in the basement of the Zagros fold and thrust belt. *Journal of Petroleum Geology*, 24, 5–28.
- Hinsch, R., & Bretis, B. (2015). A semi-balanced section in the northwestern Zagros region: Constraining the structural architecture of the Mountain Front Flexure in the Kirkuk Embayment, Iraq. *GeoArabia*, 20(4), 41–62.
- Homke, S., Verges, J., Serra-Kiel, J., Bernalda, G., Sharp, I., Garces, M., et al. (2009). Late Cretaceous-Paleocene formation of the proto-Zagros foreland basin, Lorestan Province, SW Iran. *Geological Society of America Bulletin*, 121, 963–978.
- Ishii, M., Shearer, P. M., Houston, H., & Vidale, J. E. (2005). Extent, duration and speed of the 2004 Sumatra-Andaman earthquake imaged by the Hi-Net array. *Nature*, 435, 933–936.
- Ji, C., Helmberger, D. V., Wald, D. J., & Ma, K.-F. (2003). Slip history and dynamic implications of the 1999 Chi-Chi, Taiwan, earthquake. *Journal of Geophysical Research*, 108(B9), 2412. <https://doi.org/10.1029/2002JB001764>
- Ji, C., Wald, D. J., & Helmberger, D. V. (2002). Source description of the 1999 Hector Mine, California earthquake; Part I: Wavelet domain inversion theory and resolution analysis. *Bulletin of the Seismological Society of America*, 92(4), 1192–1207.
- Jónsson, S., Zebker, H., Segall, P., & Amelung, F. (2002). Fault slip distribution of the 1999 M_w 7.1 Hector Mine, California, Earthquake, estimated from satellite radar and GPS measurements. *Bulletin of the Seismological Society of America*, 92, 1377–1389.
- Jordan, T. H., & Sverdrup, K. A. (1981). Teleseismic location techniques and their application to earthquake clusters in the South-Central Pacific. *Bulletin of the Seismological Society of America*, 71, 1105–1130.
- Kanamori, H., & Anderson, D. L. (1975). Theoretical basis of some empirical relations in seismology. *Bulletin of the Seismological Society of America*, 65, 1073–1095.
- Karasözen, E., Nissen, E., Bergman, E. A., & Ghods, A. (2017). Seismotectonics of the Zagros (Iran) from orogen-wide earthquake relocations. In *AGU Fall Meeting Abstract* (pp. T41A-0590). New Orleans.
- Karasözen, E., Nissen, E., Bergman, E. A., Johnson, K. L., & Walters, R. J. (2016). Normal faulting in the Simav graben of western Turkey reassessed with calibrated earthquake relocations. *Journal of Geophysical Research: Solid Earth*, 121, 4553–4574. <https://doi.org/10.1002/2016JB012828>
- Karasözen, E., Nissen, E., Büyükkapınar, P., Cambaz, M. D., Kahraman, M., Ertan, E. K., et al. (2018). The 2017 July 20 M_w 6.6 Bodrum–Kos earthquake illuminates active faulting in the Gulf of Gökova, SW Turkey. *Geophysical Journal International*, 214(1), 185–199.
- Kent, P. E. (1979). The emergent Hormuz salt plugs of southern Iran. *Journal of Petroleum Geology*, 2, 117–144.
- Koshnaw, R. I., Horton, B. K., Stockli, D. F., Barber, D. E., Tamar-Agha, M. Y., & Kendall, J. J. (2017). Neogene shortening and exhumation of the Zagros fold-thrust belt and foreland basin in the Kurdistan region of northern Iraq. *Tectonophysics*, 694, 332–355.
- Koyi, H. A., Hessami, K., & Teixell, A. (2000). Epicenter distribution and magnitude of earthquakes in fold-thrust belts: Insights from Sandbox Models. *Geophysical Research Letters*, 27, 273–276.
- Langston, C. A., & Helmberger, D. V. (1975). A procedure for modelling shallow dislocation sources. *Geophysical Journal of the Royal Astronomical Society*, 42(1), 117–130.
- Lohman, R. B., & Barnhart, W. D. (2010). Evaluation of earthquake triggering during the 2005–2008 earthquake sequence on Qeshm Island, Iran. *Journal of Geophysical Research*, 115, B12413. <https://doi.org/10.1029/2010JB007710>
- Lohman, R. B., & Simons, M. (2005). Locations of selected small earthquakes in the Zagros Mountains. *Geochemistry, Geophysics, Geosystems*, 6, Q03001. <https://doi.org/10.1029/2004GC000849>
- Maggi, A., Jackson, J. A., Priestley, K., & Baker, C. (2000). A re-assessment of focal depth distributions in southern Iran, the Tien Shan and northern India: Do earthquakes really occur in the continental mantle? *Geophysical Journal International*, 143, 629–661.
- Maggi, A., Priestley, K., & Jackson, J. (2002). Focal depths of moderate and large size earthquakes in Iran. *Journal of Seismology and Earthquake Engineering*, 4(2–3), 1–10.
- Maheri-Peyrov, M., Ghods, A., Abbasi, M., Bergman, E., & Sobouti, F. (2016). M_L shear wave velocity tomography for the Iranian Plateau. *Geophysical Journal International*, 205, 179–191.
- Masson, F., Chéry, J., Hatzfeld, D., Martinod, J., Vernant, P., Tavakoli, F., & Ghafory-Ashtiani, M. (2005). Seismic versus aseismic deformation in Iran inferred from earthquakes and geodetic data. *Geophysical Journal International*, 160, 217–226.
- McCaffrey, R., & Abers, G. (1988). SYN3: A program for inversion of teleseismic body wave forms on microcomputers. Massachusetts: Hanscomb Air Force Base. Air force geophysical laboratory technical report.
- McCaffrey, R., Zwick, P., & Abers, G. (1991). SYN4 program (*Tech. rep.*): IASPEI Software Library.
- McKenzie, D. (1972). Active tectonics of the Mediterranean region. *Geophysical Journal International*, 30, 109–185.
- McQuarrie, N. (2004). Crustal scale geometry of the Zagros fold-thrust belt, Iran. *Journal of Structural Geology*, 26, 519–535.
- Meade, B. J. (2007). Algorithms for the calculation of exact displacements, strains, and stresses for triangular dislocation elements in a uniform elastic half space. *Computers & Geosciences*, 33, 1064–1075.
- Molnar, P., & Lyon-Caen, H. (1989). Fault plane solutions of earthquakes and active tectonics of the Tibetan Plateau and its margins. *Geophysical Journal International*, 99, 123–154.
- Motaghi, M., Bahroudi, A., Haghghi, M. H., Samsonov, S., Fielding, E., & Wetzel, H.-U. (2015). The 18 August 2014 M_w 6.2 Mormori, Iran, Earthquake: A Thin-Skinned Faulting in the Zagros Mountain Inferred from InSAR Measurements. *Seismological Research Letters*, 86(3), 775–782.
- Motaghi, K., Shabaniyan, E., & Kalvandi, F. (2017). Underplating along the northern portion of the Zagros suture zone, Iran. *Geophysical Journal International*, 210, 375–389.

- Motaghi, K., Shabaniyan, E., Tatar, M., Cuffaro, M., & Doglioni, C. (2017). The south Zagros suture zone in teleseismic images. *Tectonophysics*, *694*, 292–301.
- Nealy, J. L., Benz, H. M., Hayes, G. P., Bergman, E. A., & Barnhart, W. D. (2017). The 2008 Wells, Nevada, earthquake sequence: Source constraints using calibrated multiple-event relocation and InSAR. *Bulletin of the Seismological Society of America*, *107*(3), 1107–1117.
- Nealy, J. L., Herman, M. W., Moore, G. L., Hayes, G. P., Benz, H. M., Bergman, E. A., Barrientos, S. E. (2017) Valparaíso earthquake sequence and the megathrust patchwork of central Chile. *Geophysical Research Letters*, *44*, 8865–8872. <https://doi.org/10.1002/2017GL074767>
- Ni, J., & Barazangi, M. (1986). Seismotectonics of the Zagros continental collision zone and a comparison with the Himalayas. *Journal of Geophysical Research*, *91*, 8205–8218.
- Nippres, S. E. J., Heyburn, R., & Walters, R. J. (2017). The 2008 and 2012 Moosiyán earthquake sequences: Rare insights into the role of strike slip and thrust faulting within the simply folded belt (Iran). *Bulletin of the Seismological Society of America*, *107*(4), 1625–1641.
- Nissen, E., Ghorashi, M., Jackson, J., Parsons, P., & Talebian, M. (2007). The 2005 Qeshm Island earthquake (Iran)—A link between buried reverse faulting and surface folding in the Zagros Simply Folded Belt? *Geophysical Journal International*, *171*, 326–338.
- Nissen, E., Jackson, J., Jahani, S., & Tatar, M. (2014). Zagros “phantom earthquakes” reassessed—The interplay of seismicity and deep salt flow in the Simply Folded Belt? *Journal of Geophysical Research: Solid Earth*, *119*, 3561–3583. <https://doi.org/10.1002/2013JB010796>
- Nissen, E., Tatar, M., Jackson, J. A., & Allen, M. B. (2011). New views on earthquake faulting in the Zagros fold-and-thrust belt of Iran. *Geophysical Journal International*, *186*, 928–944.
- Nissen, E., Yamini-Fard, F., Tatar, M., Gholamzadeh, A., Bergman, E., Elliott, J. R., et al. (2010). The vertical separation of mainshock rupture and microseismicity at Qeshm Island in the Zagros Simply Folded Belt, Iran. *Earth and Planetary Science Letters*, *296*, 181–194.
- Obaid, A. K., & Allen, M. B. (2017). Landscape maturity, fold growth sequence and structural style in the Kirkuk Embayment of the Zagros, northern Iraq. *Tectonophysics*, *717*, 27–40.
- Okada, Y. (1985). Surface deformation due to shear and tensile faults in a half-space. *Bulletin of the Seismological Society of America*, *75*, 1135–1154.
- Palano, M., Imprescia, P., Agnon, A., & Gresta, S. (2018). An improved evaluation of the seismic/geodetic deformation-rate ratio for the Zagros Fold-and-Thrust collisional belt. *Geophysical Journal International*, *213*, 194–209.
- Paul, A., Hatzfeld, D., Kaviani, A., Tatar, M., & Péquegnat, C. (2010). Seismic imaging of the lithospheric structure of the Zagros Mountain belt (Iran). *Geological Society, London, Special Publications*, *330*, 5–18.
- Press, W. H., Teukolsky, S. A., Vetterling, W. T., & Flannery, B. P. (1992). *Numerical recipes in C: The art of scientific computing*. Cambridge: Cambridge University Press.
- Roustaei, M., Nissen, E., Abbassi, M., Gholamzadeh, A., Ghorashi, M., Tatar, M., et al. (2010). The 25 March 2006 Fin earthquakes (Iran)—Insights into the vertical extents of faulting in the Zagros Simply Folded Belt. *Geophysical Journal International*, *181*, 1275–1291.
- Sadeghi, S., & Yassaghi, A. (2016). Spatial evolution of Zagros collision zone in Kurdistan, NW Iran: Constraints on Arabia-Eurasia oblique convergence. *Solid Earth*, *7*, 659–672.
- Schimmel, M., & Paulssen, H. (1997). Noise reduction and detection of weak, coherent signals through phase-weighted stacks. *Geophysical Journal International*, *130*, 497–505.
- Sepehr, M., & Cosgrove, J. (2004). Structural framework of the Zagros Fold–Thrust Belt, Iran. *Marine and Petroleum Geology*, *21*, 829–843.
- Sepehr, M., Cosgrove, J., & Moieni, M. (2006). The impact of cover rock rheology on the style of folding in the Zagros fold-thrust belt. *Tectonophysics*, *427*, 265–281.
- Shahvar, M. P., Zare, M., & Castellaro, S. (2013). A unified seismic catalog for the Iranian plateau (1900–2011). *Seismological Research Letters*, *84*(2), 233–249.
- Sherkati, S., & Letouzey, J. (2004). Variation of structural style and basin evolution in the central Zagros (Izeh zone and Dezful Embayment), Iran. *Marine and Petroleum Geology*, *21*, 535–554.
- Sherkati, S., Letouzey, J., & Frizon de Lamotte, D. (2006). Central Zagros fold-thrust belt (Iran): New insights from seismic data, field observation, and sandbox modeling. *Tectonics*, *25*, TC4007. <https://doi.org/10.1029/2004TC001766>
- Talebian, M., & Jackson, J. (2004). A reappraisal of earthquake focal mechanisms and active shortening in the Zagros Mountains of Iran. *Geophysical Journal International*, *156*, 506–526.
- Taymaz, T., Jackson, J., & McKenzie, D. (1991). Active tectonics of the north and central Aegean Sea. *Geophysical Journal International*, *106*, 433–490.
- Teknik, V., & Ghods, A. (2017). Depth of magnetic basement in Iran based on fractal spectral analysis of aeromagnetic data. *Geophysical Journal International*, *209*, 1878–1891.
- Vajedian, S., Motagh, M., Mousavi, Z., Motaghu, K., Fielding, E. J., Akbari, B., et al. (2018). Coseismic deformation field of the M_w 7.3 12 November 2017 Sarpol-e Zahab (Iran) Earthquake: A decoupling horizon in the Northern Zagros Mountains inferred from InSAR observations. *Remote Sensing*, *10*, 1589.
- Vergés, J., Goodarzi, M. G. H., Emami, H., Karpuz, R., Efstathiou, J., & Gillespie, P. (2011). Multiple detachment folding in Pusht-e Kuh Arc, Zagros: Role of mechanical stratigraphy. In K. McClay, J. H. Shaw, & J. Suppe (Eds.), *Thrust fault related folding*: American Association of Petroleum Geologists, pp. 69–94.
- Vergés, J., Saura, E., Casciello, E., Fernández, M., Villaseñor, A., Jiménez-Munt, I., & Garcia-Castellanos, D. (2011). Crustal-scale cross-sections across the NW Zagros belt: Implications for the Arabian margin reconstruction. *Geological Magazine*, *148*, 739–761.
- Vernant, P., Nilforoushan, F., Hatzfeld, D., Abbassi, M. R., Vigny, C., Masson, F., et al. (2004). Present-day crustal deformation and plate kinematics in the Middle East constrained by GPS measurements in Iran and northern Oman. *Geophysical Journal International*, *157*, 381–398.
- Walker, R. T., Bergman, E. A., Szeliga, W., & Fielding, E. J. (2011). Insights into the 1968–1997 Dasht-e Bayaz and Zirkuh earthquake sequences, eastern Iran, from calibrated relocations, InSAR and high-resolution satellite imagery. *Geophysical Journal International*, *187*, 1577–1603.
- Walpersdorf, A., Hatzfeld, D., Nankali, H., Tavakoli, F., Nilforoushan, F., Tatar, M., et al. (2006). Difference in the GPS deformation pattern of North and Central Zagros (Iran). *Geophysical Journal International*, *167*, 1077–1088.
- Wessel, P., Smith, W. H. F., Scharroo, R., Luis, J., & Wobbe, F. (2013). Generic Mapping Tools: Improved version released. *Eos, Transactions American Geophysical Union*, *94*, 409–410.

- Wright, T. J., Lu, Z., & Wicks, C. (2003). Source model for the M_w 6.7, 23 October 2002, Nenana Mountain Earthquake (Alaska) from InSAR. *Geophysical Research Letters*, *30*(18), 1974. <https://doi.org/10.1029/2003GL018014>
- Wright, T. J., Parsons, B. E., Jackson, J. A., Haynes, M., Fielding, E. J., England, P. C., & Clarke, P. J. (1999). Source parameters of the 1 October 1995 Dinar (Turkey) earthquake from SAR interferometry and seismic bodywave modelling. *Earth and Planetary Science Letters*, *172*, 23–37.
- Zhang, H., & Ge, Z. (2010). Tracking the rupture of the 2008 Wenchuan earthquake by using the relative back-projection method. *Bulletin of the Seismological Society of America*, *100*, 2551–2560.
- Zwick, P., McCaffrey, R., & Abers, G. (1994). MT5 program. *IASPEI Software Library*, *4*.